Chemical Engineering Journal 405 (2021) 126651

Contents lists available at ScienceDirect

Chemical Engineering Journal

journal homepage: www.elsevier.com/locate/cej

Graphene-TiO_2 hybrids for photocatalytic aided removal of VOCs and nitrogen oxides from outdoor environment

D.M. Tobaldi[a,*], D. Dvoranová[b], L. Lajaunie[c,d], N. Rozman[e], B. Figueiredo[f], M.P. Seabra[a], A. Sever Škapin[e], J.J. Calvino[c,d], V. Brezová[b], J.A. Labrincha[a]

[a] Department of Materials and Ceramic Engineering and CICECO–Aveiro Institute of Materials, University of Aveiro, Campus Universitário de Santiago, 3810–193 Aveiro, Portugal
[b] Institute of Physical Chemistry and Chemical Physics, Faculty of Chemical and Food Technology, Slovak University of Technology in Bratislava, Radlinského 9, Bratislava SK-812 37, Slovak Republic
[c] Departamento de Ciencia de los Materiales e Ingeniería Metalúrgica y Química Inorgánica, Facultad de Ciencias, Universidad de Cádiz, Campus Río San Pedro S/N, Puerto Real 11510, Cádiz, Spain
[d] Instituto Universitario de Investigación de Microscopía Electrónica y Materiales (IMEYMAT), Facultad de Ciencias, Universidad de Cádiz, Campus Río San Pedro S/N, Puerto Real 11510, Cádiz, Spain
[e] Slovenian National Building and Civil Engineering Institute, Dimičeva 12, 1000 Ljubljana, Slovenia
[f] Graphenest, Lugar da Estação, Edifício Vouga Park, 3740–070 Paradela do Vouga, Portugal

HIGHLIGHTS

- High throughput low-cost sol–gel graphene-TiO_2 nanocomposites.
- EPR proved different radicals upon excitation: complex reaction pathways.
- Stable and high performance photocatalytic removal of VOCs and NO_x.
- 1 wt% graphene gave 2-fold increase in photocatalytic VOCs & NO_x removal.
- Graphene to increase electric transport; decrease exciton recombination.

GRAPHICAL ABSTRACT

ARTICLE INFO

Keywords:
Air pollution
Volatile organic compounds
Nitrogen oxides
Graphene
Solar photochemical reaction

ABSTRACT

Outdoor and indoor air pollution has become a global concern in modern society. Although many policies and regulations on air quality have been promulgated worldwide over the past decades, airborne pollution still negatively affects health and therefore the life-style of human beings. One of the strategies to challenge this problem might be reducing the amount of airborne pollutant by mineralising them *via* photoinduced reactions. Photocatalytic oxidation of gaseous pollutants *via* titanium dioxide is one of the most promising solar photochemical reactions. In this research work, by means of a green sol–gel procedure, we have coupled titania to graphene (0.5 and 1.0 wt%) aiming to increase the solar photocatalytic activity of the produced hybrid materials. Transient paramagnetic species formed upon UV-A irradiation were detected by means of EPR spectroscopy. The photocatalytic reactions were assessed by monitoring the removal of nitrogen oxides and two different volatile organic compounds (benzene and isopropanol), which has never been assessed before. Our results highlight the exceptional characteristics of the TiO_2/graphene hybrid material synthesised with 1.0 wt% graphene, and its excellent suitability for multi-purpose applications in the field of environmental remediation. Compared to unmodified titania, it shows a clear enhancement in the photocatalytic removal of those hazardous

* Corresponding author.
E-mail addresses: david.tobaldi@ua.pt, david@davidtobaldi.org (D.M. Tobaldi).
@D14MT (D.M. Tobaldi)

https://doi.org/10.1016/j.cej.2020.126651
Received 15 June 2020; Received in revised form 16 July 2020; Accepted 10 August 2020
Available online 13 August 2020

pollutants, having a photocatalytic degradation rate twice higher. In addition, the same material is highly stable and shows fully recyclability over repeated tests. Hybrid titania-graphene materials could thus be exploited to grant safer outdoor and indoor environments, having thus a beneficial impact on public health and on the quality of our lives.

1. Introduction

Air pollution is defined by the World Health Organisation as: "*contamination of the indoor or outdoor environment by any chemical, physical or biological agent that modifies the natural characteristics of the atmosphere*" [1]. Seinfeld and Pandis proposed an extended definition, stating that: "*air pollution is the presence in the air of one or more substances at a concentration or for duration above their natural levels, with the potential to produce an adverse effect*" [2]. This implies that some of the substances that are regarded to be "air pollutant", are naturally present in the air [3]. Those air pollutants have both natural and anthropogenic origin. Indeed, anthropogenic activity has had, and is still having, a dominant role in the increase of air pollutants to levels that yield adverse impact on human health and on the environment. Exposure to air pollution has been reported to be as the 5th ranking human health risk factor worldwide [4]. Several studies also recognised an association between air pollution and the climate changes that we are idly witnessing [5].

Common (indoor and outdoor) anthropogenic air pollutants are: particulate matter (PM), nitrogen oxides (NO_x), and volatile organic compounds (VOCs). PM air pollution is given by a mixture of microscopic solid particles and liquid droplets – PM with an aerodynamic diameter equal to, or smaller than, 10 and 2.5 μm is named PM_{10} and $PM_{2.5}$, respectively [6]. NO_x emissions originate themselves from the combustion processes in stationary and mobile units [7], thus they are commonly related to traffic-sources – incidentally, around 80% of the NO_x emitted by automobiles comes from diesel-powered ones [8]. It is interesting to note that the lockdown for COVID-19 in Italy lead to a significant reduction of pollutants concentration, mainly due to vehicular traffic (PM_{10}, $PM_{2.5}$, benzene, CO, and NO_x) [9]. NO_x are related to several short- and long-term health effects [10], even to carcinogenicity [11]. VOCs are defined, according to the directive from the European Union, as: "*any organic compounds having at 293.15 K a vapour pressure of 0.01 kPa or more, or having a corresponding volatility under the particular conditions of use*".[12] Anthropogenic VOCs emission was estimated to be around 142 $Tg.C.yr^{-1}$ in the atmosphere [13]. Moreover, ground-level ozone (O_3) is formed by photochemical reactions between sunlight and NO_x and VOCs [14], giving rise to the so-called *photochemical smog*, this again having an adverse impact on human health and climate. Rubber and paint production plants, varnishes, households products are amongst the main sources of isopropanol (2-propanol, IPA) [15]. The majority of IPA exposures are unintentional and are related to the central nervous system and respiratory depression [16]. Benzene can be found primarily outdoor, due to traffic sources [17]. Toxicity of this VOC involves both bone marrow depression and leukemogenesis [18].

Given this context, it is imperative to significantly reduce this global threat. Thus, renewable sources of energy are becoming more relevant. Among those, solar energy is taking an increasingly important role. Photocatalysis is one of the most investigated solar (photo)reactions, as it has different levels of applications, ranging from water and air purification, hygiene and sanitation, environmental remediation, automotive industry [19]. The term photocatalysis defines the acceleration of a photoreaction by a material, the (photo)catalyst, that it is not consumed during said reaction [20]. Semiconductors are the materials used as (heterogeneous) photocatalyst. Amid those photocatalytic semiconductors, titanium dioxide (titania, TiO_2), an Earth-abundant material, is one of the most promising candidates, as it possesses: high oxidising power and resistance to photocorrosion in water environment, non-toxicity, cost-effectiveness [21]. However, one of TiO_2's drawback is the relatively high recombination rate of the photogenerated exciton, dissipating the energy as light or heat, thus strongly reducing the resulting photocatalytic activity [22]. Coupling/modifying TiO_2 with other semiconductors, metals, noble-metals has been proposed to improve the spatial charge carrier separation, thus increasing the quantum yield of the photocatalytic process [23].

In 2004, Novoselov and Geim extracted from graphite a single layer of carbon atoms tightly packed into a two-dimensional honeycomb crystal structure [24]. This discovery led to the spark of the graphene-driven "*gold rush*", as the discoverers themselves dubbed graphene to be the "*rising star on the horizon of materials science and condensed matter physics*" [25]. Indeed, as of 2004, there has been remarkable progress in graphene research, quicker than that of any other material [26]. Graphene and titania can be combined [27], and their hybridisation results in a built-in electric field that increases the conductivity of that system by promoting interfacial charge transfer and separation [28]. That is a decrease in the recombination rate of the photogenerated exciton (a critical step for a photocatalytic reaction), which in turn enhances the photocatalytic activity of the material. This led to massive research focussed on graphene-TiO_2 composite materials for environmental applications [29–32]. However, the vast majority of the literature deals with photocatalytic water treatment [33–36], as only few papers, in recent literature based on graphene-TiO_2 composites, are about the photocatalytic degradation of air pollutants. Those latter works deal or with the abatement of nitrogen oxide(s) [37], or with the removal of organic compounds – like acetone [38], or benzene [39]. Still, a single comprehensive study dealing with the gas–solid phase photocatalytic removal of different kinds of hazardous organic compounds (*i.e.* alcohol and aromatic compounds), and inorganic nitrogen compounds (*i.e.* NO and NO_2) over graphene/TiO_2 hybrid materials has never been assessed before. To fill that literature gap, in this paper we have used a green sol–gel synthesis method to produce TiO_2 and hybrid TiO_2/graphene nanostructures [40]. Their photocatalytic activity was assessed in the gas phase, by monitoring the degradation of NO_x and two different types of VOCs, namely: benzene and IPA. The light source used in the photocatalytic experiments imitated the solar spectrum, so as to reproduce an outdoor environment. However, an artificial visible light emitting diode (LED) lamp – *i.e.* a lamp with no UV components, thus imitating and indoor environment, was also used in the photocatalytic tests. Results showed that the addition of graphene boosted titania's photocatalytic activity. With 1.0 wt% graphene, and using a light imitating the solar spectrum, the photocatalytic activity of TiO_2 was (more than) doubled in NO_x abatement, benzene removal, and IPA oxidation, never being reported before. Materials produced in this research work possess high throughput against those hazardous pollutants, therefore, being excellent candidates for offering a safer outdoor environment.

2. Experimental section

2.1. Sample preparation

We followed an aqueous sol–gel procedure for the synthesis of TiO_2-based photocatalytic materials; details of the synthesis can be found in a paper previously described by the authors [40]. Briefly, aqueous sols were made by means of the controlled hydrolysis and peptisation of titanium(IV)isopropoxide [Ti-*i*-pr, $Ti(OCH(CH_3)_2)_4$] with Milli-Q water (18.2 MΩ.cm, H_2O:Ti-*i*-pr = 4:1) diluted in isopropyl alcohol (2-

propanol, IPA). To make the graphene-modified TiO_2 sols, 0.5 and 1.0 wt% of graphene nanoplatelets dispersed in ethanol (supplied by Graphenest) were added to the TiO_2-based sol when this had 1 M concentration. The sols were dried in an oven at 80 °C, and then the dried gels were thermally treated under static air atmosphere using an electric muffle furnace, following thermal cycles reaching two maximum temperatures: (i) 250 °C with a heating rate of 15 °C.min^{-1}, preheating the furnace at 200 °C, with a 8 h dwell time; (ii) 450 °C, with a heating rate of 5 °C.min^{-1}, with 2 h dwell time. Specimens were referred to as: **G*x*/*Y*** were × stands for the graphene wt% (0.5 or 1.0 wt %), and *Y* is a number indicating the maximum temperature reached (*i.e.* 250 or 450 °C). For instance, the TiO_2 sol in which was added 0.5 wt% graphene, and thermally treated at 450 °C / 2 h, will be referred to as: **G0.5/450**. Unmodified titania has been labelled: **Ti250** or **Ti450**, according to the maximum temperature reached.

2.2. Sample characterisation

X-ray powder diffraction (XRPD) was used to reveal the mineralogical composition of the prepared specimens. The relative fractions of crystalline phases were determined *via* Rietveld refinements of the XRPD data. The XRPD patterns were collected at room temperature on a θ/θ diffractometer (PANalytical X'Pert Pro, NL), equipped with a fast RTMS detector (PIXcel 1D, PANalytical), with Cu K_α radiation (45 kV and 40 mA, 20–80 °2θ range, with a virtual step scan of 0.02 °2θ, and virtual time per step of 200 s). The Rietveld data analysis for obtaining semi-quantitative phase analysis (QPA) information was assessed using the GSAS-EXPGUI software packages [41,42]. The instrumental broadening was obtained from the refinement of LaB_6 standard (NIST SRM 660b) and included in all of the Rietveld refinements. The refinement strategy that we followed has been reported in a previous work [40]. XRPD was also used to gain microstructural information. At this purpose, the same instrument and setup as per the QPA was employed, but XRPD patterns were recorded in the 20–145 °2θ range, with a virtual step-scan of 0.1 °2θ, and virtual time per step of 500 s, so to work with data having a higher signal-to-noise ratio. The whole powder pattern modelling (WPPM) [43], as implemented in the PM2K software package [44], was used for the microstructural analysis of the diffraction data. In this work we adopted the same modelling approach as that described in previous works of us, assuming the crystalline domains to be spherical, and their diameter distributed according to a log-normal curve [40].

High-resolution scanning transmission electron microscopy (HR-TEM) imaging and electron energy-loss spectroscopy analysis (SR-EELS) were performed using a FEI Titan Cubed Themis microscope operated at 80 kV. This microscope is equipped with a double Cs aberration-corrector, a monochromator, a X-FEG gun, an ultrahigh resolution energy filter (Gatan Quantum ERS), which allows working in dual-EELS mode, and a super X EDS detector. The monochromator was excited during imaging and spectroscopic experiments to minimize chromatic aberrations. Convergence and collection angles during EELS experiments were 5 and 21 mrad, respectively. The probe diameter for EELS acquisition in TEM mode was around 30 nm. The energy resolution, measured as the full width at half maximum of the zero loss peak, was 0.75 eV with a dispersion of 0.25 eV.pixel^{-1}. Background subtraction for the core-loss spectra was performed by using the usual inverse power law function. Interpretations of the fast Fourier transform (FFT) patterns in HR-TEM images were performed by using the JEMS software [45].

Optical spectra of the prepared graphene-TiO_2 hybrid materials were recorded on a Shimadzu UV-3100 spectrometer (JP), equipped with an integrating sphere, and a white reference material made of Spectralon; UV − vis spectral range was explored (250–850 nm), using 0.2 nm in resolution. Raman spectra were acquired on a RFS 100/S (Bruker, DE) equipped with a 1,064 nm Nd:YAG laser as the excitation source, in the 50–1,800 cm^{-1} wavenumber range, with 2 cm^{-1} in resolution. Specific surface area (SSA) of the specimens was measured by means of the Brunauer–Emmett–Teller (BET) method (Micromeritics Gemini 2380, US) using N_2 as the adsorbate gas, on samples degassed at 120 °C.

EPR spin trapping experiments were performed using the spin trapping agent 5,5-dimethyl-1-pyrroline *N*-oxide (DMPO; Sigma-Aldrich, distilled prior to the application). Benzene (anhydrous, 99.8%) and 2-propanol (IPA, puriss. p.a., ACS reagent, ≥99.8%) were purchased from Sigma-Aldrich. The DMPO solutions in benzene and IPA (0.2 M) were used to impregnate the powdered photocatalysts placed in a thin-walled quartz Q-band EPR tube (Bruker). As-prepared photocatalyst was mixed by a gentle stream of argon in order to reduce the concentration of dissolved oxygen, and to eliminate the EPR line broadening in benzene and IPA caused by oxygen dissolved in these solvents [46]. The sample was directly irradiated in the cavity of EPR spectrometer EMX (Bruker) operating at 100 kHz field modulation in the standard TE_{102} rectangular cavity (ER 4102 ST, Bruker) at room temperature. An UV radiator [λ_{max} = 365 nm; Bluepoint LED, Hönle UV Technology; irradiance of 15 mW.cm^{-2} within the EPR cavity determined by a UVX radiometer (UVP, USA)] was used as irradiation source. The standard EPR spectrometer settings were as follows: microwave frequency: ~9.447 GHz; microwave power: 11.5 mW; center field: 363 mT; gain: 1 × 10^5; modulation amplitude: 0.05 mT; sweep time: 25 s; time constant: 10.24 ms; number of scans: 10. The experimental EPR spectra were analysed by the WinEPR software (Bruker), and the simulated spectra were calculated with the EasySpin toolbox working under Matlab (MathWorks) software [47].

2.3. Functional properties: Photocatalytic experiments

De-NO_x and benzene removal gas–solid phase photocatalytic experiments were carried out in the same reactor, that operated in continuous mode [48]. It comprised a cylindrical chamber (3.8 L internal volume) built from a high grade stainless steel with a stainless steel top with a sealed glass window to allow the light to reach the sample that was placed inside – a scheme of the reactor employed is displayed in Figure S1a of the Supplementary information file. A light imitating the solar spectrum (Osram Ultra-Vitalux, 300 W) was used as light source. This was positioned 33 cm above the photocatalyst; the radiant flux per unit area (irradiance) reaching the surface of the photocatalyst was then equal to 3.5 mW.cm^{-2} in the UV-A range, and 35 mW.cm^{-2} in the visible spectral range – values measured with a radiometer (Delta OHM, HD2302.0, IT). A LED lamp (Philips warm white, 2700 K LED bulb, 9.5 W) was employed to mimic an indoor environment. The LED was placed 12 cm above the photocatalyst. The irradiance reaching the photocatalyst was estimated to be approximately 5.8 mW.cm^{-2} in the visible-light range and nil in the UV-A range. Emission spectra of the solar and visible-light LED lamps are displayed in Figure S2.

A Petri dish, 6 cm in diameter, was covered with a layer of photocatalyst (0.10 g). The tests were performed at 24 ± 1 °C (temperature inside the reactor) with a relative humidity of 36%. These parameters were controlled by a thermocouple that was placed inside the chamber, and a humidity sensor placed in the inlet pipe, and they were stable throughout the tests.

As per the de-NO_x photocatalytic experiments, the initial concentration of NO_x (prepared using synthetic air and NO_x gas) was set at 200 ppb. That concentration is higher than that commonly reported outdoor, *e.g.* outdoor urban levels have an annual mean range of 11–48 ppb (around 20–90 μg.m^{-3}) [49]. However, the safety limit of 200 μg.m^{-3} (approximately 110 ppb) on a daily basis is often breached in many European Countries [50].

The outlet concentration of NO_x gases was measured using a chemiluminescence analyser (AC-31 M, Environment SA, FR), according to a procedure that we described in very detail previously [51,52].

When benzene was used as model gas, its concentration exiting through the outlet was measured using a VOC-72 M gas analyser

(Environment SA, FR), that is based on gas chromatography and photoionisation detector. The inlet gas mixture (prepared mixing gas cylinders containing synthetic air and benzene) was allowed to flow into the chamber until it stabilised at a concentration of ~ 260 $\mu g.m^{-3}$ (~80 ppb). This concentration was chosen because the World Health Organisation recommends an exposure to total VOCs < 300 $\mu g.m^{-3}$ during 8 h/day [53]. The mixture of air with that concentration of benzene was guaranteed using two mass flow controllers with a flow rate of 150 $mL.min^{-1}$. The photocatalytic experiments were assessed by placing the photocatalyst inside the reactor and covering the glass window. Once the desired NO_x/benzene concentration was reached and it attained a stable level into the reactor, the window glass was uncovered, the lamp turned on, and the photocatalytic reaction started. Photocatalytic activity for de-NO_x abatement and benzene removal was reported as formal quantum efficiency (FQE) [54], defined as the number of molecules degraded per incident photon. In this work, based on the results obtained in *Section 3.2* in which the optical band-gap was determined, we presumed that prepared photocatalysts exploited the UV–A part of the electromagnetic spectrum (*i.e.* 315–400 nm) for band-to-band excitation, thus excluding wavelengths > 400 nm. Furthermore, aiming to have a better comparison between the tested specimens, data relative to the first 2 min (de-NO_x) or 60 min (benzene removal) of reaction time, were interpreted according to a first-order kinetic law.

A different reactor was employed for the gas-phase oxidation of IPA and, unlike the reactor described previously, this was a batch system (Figure S1b). It was a cylindrical reactor (1.4 L in volume) covered by a quartz glass connected by Teflon tubes to a FT-IR spectrometer; the whole batch system was hermetically sealed. IPA photocatalytic oxidation is as follows: IPA $\xrightarrow{k_1}$ acetone $\xrightarrow{k_2}$ further products $\rightarrow CO_2 + H_2O$. Following the works of Munuera and co-authors [55,56], the IPA to acetone reaction is described as a zero order reaction, whilst the second reaction (acetone to further products) is a first order reaction. Also, Larson *et al.* [57], demonstrated that $k_1 \gg k_2$, therefore, we can genuinely assume the initial reaction rate of acetone formation to be reasonably approximated as linear, and obtain a reliable kinetic for the photocatalytic activity. The working distance between the Petri dish and the lamp was 6 cm. The light source employed for the photocatalytic tests was a 300 W Xenon lamp (Newport Oriel Instruments, US). The lamp imitates the solar light spectrum, both in the UV and visible range, with an irradiance of approximately 0.8 $mW.cm^{-2}$ in the UV range (250–400 nm), and 8.8 $mW.cm^{-2}$ in the wavelength range of 400–800 nm. A 400 nm cut-off filter was used to exclude the UV radiation, and thus measurements were also taken only under visible-light irradiation. The filter decreases the light intensity, which reaches a value of 6.5 $mW.cm^{-2}$ in the 400–800 nm range. The relative humidity in the reacting system was kept constant in the range 25%–30% by means of a flow of air passing through molecular sieves until a predefined humidity was attained. Each experiment was performed by injecting 8 μL of IPA (~800 ppm in gas phase) into the reacting system through a septum; the total reaction time was set at 24 h, and the lamp was turned on after a certain period of time after IPA injection, to allow for an adsorption/desorption equilibrium. IPA degradation, as well as the acetone formation-degradation process, was followed by monitoring the calculated area of their characteristic peaks located at 1,104 and 1,207 cm^{-1}, respectively, by using a FT-IR spectrometer (Perkin Elmer Spectrum BX, US). The acetone formation kinetics was taken as a measurement of photocatalytic activity, because the photocatalytic oxidation of IPA is the only source of acetone. Thus, although an indirect evidence, it unequivocally proves IPA oxidation. On the other hand, the decreasing concentration of IPA may be due to photocatalytic activity and some other undesired processes, like adsorption and possible minor leaking. [It has to be stressed here that the radiant fluxes (in the UV-A and visible regions) entering the reactors are significantly lower than those of xenon arc lamps that are normally used by the catalytic community – *i.e.* in the order of around 8 $mW.cm^{-2}$ in the UV-A region, and 80 $mW.cm^{-2}$ in the visible range [58–60]. All of the photocatalytic tests were repeated in triplicate to check recyclability and photostability of the photocatalysts.

3. Results and discussion

3.1. XRPD and HR-TEM analyses

XRPD patterns of the synthesised materials are shown in Figure S3a,b whilst Rietveld QPA results are listed in Table 1. A graphical output of a Rietveld refinement is in Figure S4. TiO_2 thermally treated at 250 °C / 8 h (**Ti250**) is composed of anatase (79.6 wt%), rutile (8.1 wt%), and brookite (12.3 wt%). Addition of graphene to the system strongly delayed the anatase-to-rutile phase transition (ART), being the anatase wt% amount in **G0.5/250** (**G1.0/250**): 94.2 wt% (92.8 wt%); that of rutile was: 0.6 wt% (0.4 wt%); brookite: 5.2 wt% (6.7 wt%). Similarly, graphene addition retarded the ART in the specimens thermally treated at 450 °C / 2 h. **Ti450** is composed of 70.8 wt% anatase, 19.5 wt% rutile, and 9.7 wt% brookite. Specimens **G0.5/450** (**G1.0/450**) are composed of: 89.1 wt% (88.4 wt%) anatase; rutile: 8.1 wt% (9.4 wt%); brookite: 2.8 wt% (2.1 wt%). As per the microstructure, microstructural information as extracted from the WPPM formalism is listed in Table 1 and S1, and Figure S5 (an output of a WPPM modelling is shown in Figure S6). Consistent with QPA data, graphene addition to the system delayed the nucleation-and-growth of anatase crystalline domains – ART being a nucleation-and-growth phenomenon [61]. Indeed, the diameter of anatase crystalline domains in **Ti250** is 4.4 nm. That in **G0.5/250** (**G1.0/250**) is equal to: 3.8 nm (3.9 nm). A similar behaviour happens when the specimens are thermally treated at 450 °C / 2 h: the average diameter of anatase crystalline domain in **Ti450** is 10.4 nm. That in **G0.5/450** (**G1.0/450**) is: 7.0 nm (6.2 nm). Rutile nanocrystals in **Ti450** have a diameter equal to 14.4 nm; those in **G0.5/450** (**G1.0/450**): 8.7 nm (8.3 nm) – *cf* Table 1.

TEM micrographs of pure graphene are displayed in Figure S7. Graphene flakes randomly superposed are visible in Figure S7a. Each flake is around 0.9–1.0 μm in length, and 200–300 nm in width. The thickness of each flake is around 5 nm, *cf* Figure S7b.

Fig. 1a shows a TEM image acquired on **G1.0/450**. The presence of

Table 1
Phase fraction (wt%) of TiO_2 polymorphs, average diameter of the crystalline domains, and BET specific surface area in the prepared specimens.

Sample	Phase composition (wt%)			Mean crystalline domain diameter (nm)			
	anatase	rutile	brookite	anatase	rutile	brookite	SSA_{BET} ($m^2.g^{-1}$)
Ti250/8h	79.6 ± 0.2	8.1 ± 0.3	12.3 ± 0.5	4.4 ± 0.1	8.7 ± 1.4	–	134.4 ± 2.1
G0.5/250	94.2 ± 0.1	0.6 ± 0.1	5.2 ± 0.3	3.8 ± 0.1	–	5.6 ± 0.6	139.1 ± 1.3
G1.0/250	95.3 ± 0.1	0.4 ± 0.1	4.3 ± 0.3	3.9 ± 0.1	–	4.8 ± 0.5	140.6 ± 1.3
Ti450	70.8 ± 0.1	19.5 ± 0.1	9.7 ± 0.2	10.4 ± 0.7	14.4 ± 0.6	7.0 ± 0.1	45.9 ± 0.7
G0.5/450	89.1 ± 0.1	8.1 ± 0.2	2.8 ± 0.3	7.0 ± 0.1	8.7 ± 0.1	–	50.1 ± 0.6
G1.0/450	88.4 ± 0.1	9.4 ± 0.2	2.1 ± 0.2	6.2 ± 0.2	8.3 ± 0.6	–	57.4 ± 0.6

Agreement factors of Rietveld refinements were: $R(_F^2) \leq 4.73\%$; $R_{wp} \leq 4.39\%$; $\chi^2 \leq 2.21$. There were 2285 observations for every Rietveld refinement; the number of anatase, rutile and brookite reflections was 32, 31 and 158, respectively.

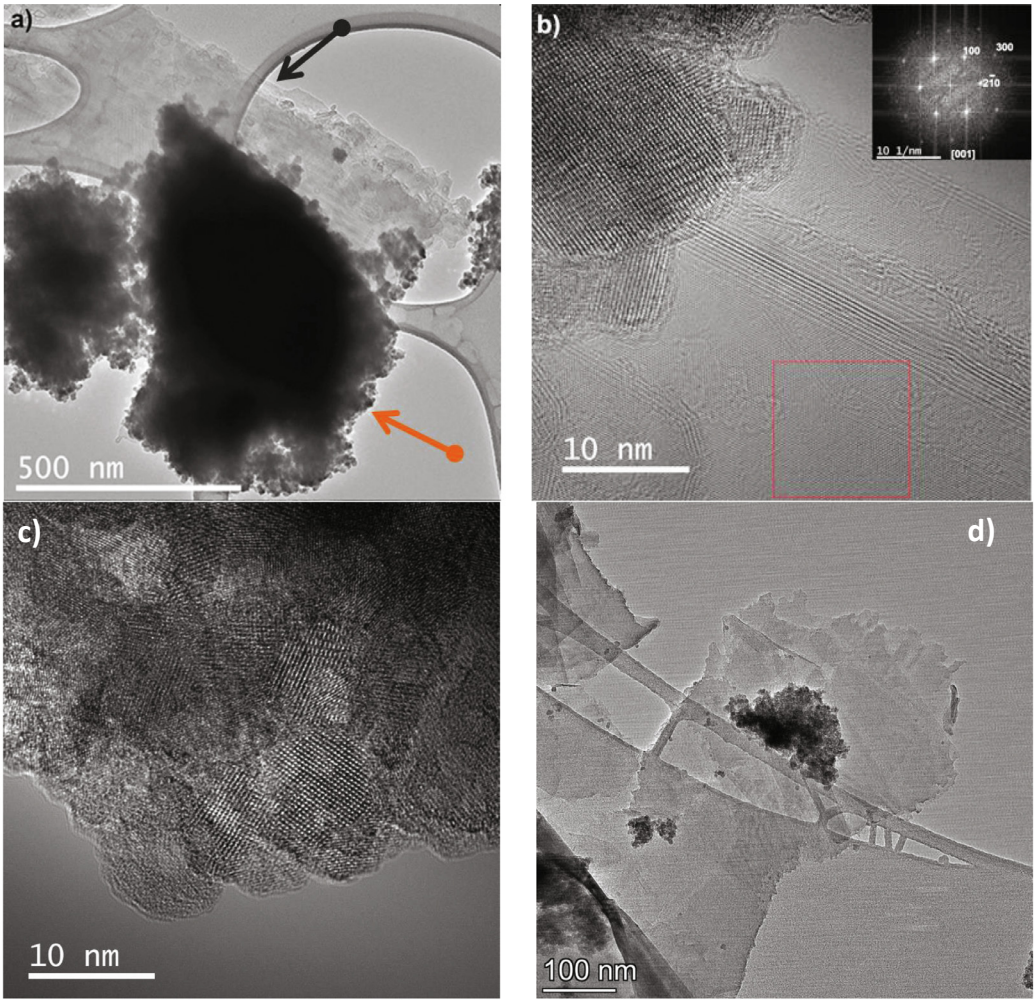

Fig. 1. a) TEM image acquired on the sample **G1.0/450**; the orange arrow points TiO_2 nanoparticles, the dark grey arrow graphene flakes. b) HR-TEM image acquired on the sample **G1.0/450**. The inset shows the FFT calculated on the area highlighted by the red square. c) HR-TEM image of **G1.0/450** to show clustered TiO_2 nanoparticles. d) TEM micrograph showing the distribution of clustered TiO_2 nanoparticles on graphene surface. (For interpretation of the references to colour in this figure legend, the reader is referred to the web version of this article.)

clustered TiO_2 nanoparticles and graphene flakes in the same area can clearly be highlighted. The flakes have a typical size of about 500 × 1000 nm. Fig. 1b depicts an image of higher magnification taken in the same area. The high crystalline quality of both the nanoparticles and the flake can be clearly highlighted. In addition, it should be noted that most of the flakes are constituted by a multi-layer graphene – the number of layers varying between 3 and ~ 20. Automatic indexation of the FFT pattern acquired on the flake show that this corresponds to a graphitic basal plane described in the [0 0 1] zone axis. TiO_2 nanoparticles are clustered, and have a typical size of about 5–7 nm, as displayed in Fig. 1c. Clustering of TiO_2 nanoparticles and their distribution over graphene's surface can be appreciated in Fig. 1d. In it, it is also shown that the thermal treatment did not virtually modify the flake structure.

To get more insight on the chemical nature of the nanostructures, EELS spectra were acquired on the flakes and nanoparticles of **G1.0/450** (Fig. 2). The EELS spectrum acquired on the nanoparticles shows the presence of Ti–$L_{2,3}$ and O–*K* edges located around 457 and 530 eV, respectively. On the other hand, the spectrum acquired on the flake shows only the presence of the C–*K* edge around 285 eV. It should be noted that no other edges, related in particular to oxygen or nitrogen, can be highlighted on the probed energy range. In addition, the C–*K* edge clearly shows fine-structure characteristics of a highly graphitic carbon [62]. These results show that the hybrid nanostructure is constituted of few-layers of graphene mixed with small TiO_2

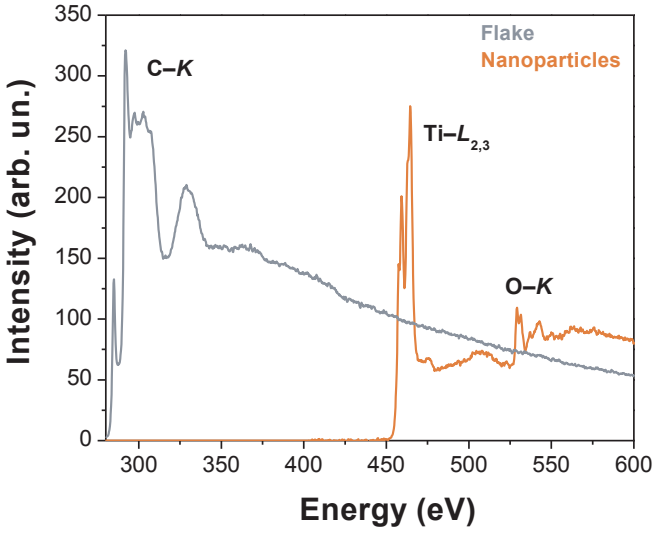

Fig. 2. EELS spectra acquired on nanoparticles (orange line) and one flake (dark blue line) in **G1.0/450**. (For interpretation of the references to colour in this figure legend, the reader is referred to the web version of this article.)

nanoparticles [62]. Similar results concerning imaging and spectroscopic analyses were obtained on **G1.0/250**.

3.2. UV–Vis and Raman spectroscopy

Diffuse reflectance (DR) spectra are shown in Fig. 3a,b. They all display one single absorption edge, located at around 380 nm, and assigned to the band-to-band transition in titania [63]. Addition of graphene increased the absorption in the visible range, consistent with previous literature reports [64]. Values of the apparent optical bandgap energy (E_g) of the specimens are listed in Table 2. These were extracted from the DR spectra by means of the Tauc-plot (considering direct and indirect interband transitions) [65], and of the differential reflectance method (Figure S8) [66]. Specimens are mostly composed of anatase (*cf* Table 1), and this TiO_2 polymorph is commonly reported to have an indirect band-to-band transition [67]. However, the E_g values determined *via* the Tauc procedure, and assuming an indirect model, are in contrast with the expected E_g value of anatase (*i.e.* ~ 3.2 eV; ~388 nm) [68]. Therefore, a direct model for interband transition would seem more appropriate in this system [see also references [39,52]] – indeed, although unusual, anatase having direct gap transition has already been reported in the literature [69,70].

However, the differential reflectance method has been reported to be a more reliable technique for extracting the E_g values in the TiO_2 polymorphs system [40,66,71]. Indeed, values listed in Table 1 (6th to 11th columns), are consistent with anatase, rutile and brookite E_gs reported in the literature [68,72].

Raman spectra are displayed in Fig. 4a,b. In this figure, the main Raman active mode of anatase are clearly detectable [*i.e.*: $E_{g(1)}$ (144 cm^{-1}); $B_{1g(1)}$ (399 cm^{-1}); A_{1g},$B_{1g(2)}$ (515 cm^{-1}); $E_{g(2)}$ (638 cm^{-1})] [73]. The major Raman bands assigned to graphene (*i.e.*: *D*, *G*, and a very weak *D'*) [74], are identified in the specimens modified with graphene (see the inset in Fig. 4a,b).

4. Functional properties: Gas-phase photocatalytic experiments

4.1. de-NO_x properties

Solar de-NO_x photocatalytic activity results are shown in Fig. 5a-d. As it is seen in Fig. 5a,b all of the specimens are able to eliminate the NO_x gases when stimulated by a light simulating the solar radiation (that is with a UV-A component). Specimens thermally treated with the two thermal cycles showed quite similar de-NO_x properties during the total duration of the experiments. This was confirmed by FQEs values too, as reported in Fig. 5c. Unmodified specimens thermally treated at 250 °C / 8 h and 450 °C / 2 h, after 10 min irradiation time, had de-NO_x removal rates equal to 6.7×10^{-3} and 9.7×10^{-1} molecules.photon^{-1}, respectively. Upon modification with 0.5 and 1.0 wt% graphene, in specimens thermally treated at 250 °C / 2 h, the FQE rates increased to 11.7×10^{-3} and 13.3×10^{-3} molecules.photon^{-1}, respectively. Better NO_x abatements FQE rates were reached when specimens were subjected to a higher thermal treatment, **G0.5/450** and **G1.0/450**, these respectively being: 12.8×10^{-3} and 14.0×10^{-3} molecules.photon^{-1}. To have a better comparison amongst the specimens, these results were compared with the initial (first 2 min of reaction) pseudo-first order kinetic constants, in which are reported the values averaged over three consecutive photocatalytic de-NO_x tests, see Fig. 5d. Indeed, specimens thermally treated at 450 °C/ 2 h exhibited a slightly better photocatalytic activity than those treated at 250 °C / 8 h. Specimens thermally treated at 450 °C / 2 h have in general a larger size of anatase and rutile crystalline domains (*cf* Table S2). This might (partly) justify the slight increase in the de-NO_x properties of those specimens: the larger the size, the lower the defect density in the material (that is: lower density of trapping centres), therefore, lower probability of the exciton recombination [75]. In any case, specimens hybridised with graphene showed a higher photocatalytic activity. Addition of 1.0 wt% graphene enhanced the photocatalytic activity: **G1.0/250** and **G1.0/450** almost doubled their photocatalytic activity compared to **Ti250** and **Ti450**. Values of the initial k'_{app} for **Ti250** and **Ti450** were 6.9×10^{-2} and 7.1×10^{-2} min^{-1}, respectively. Those of **G1.0/250** and **G1.0/450**: 11.4×10^{-2} and 12.7×10^{-2} min^{-1}, respectively. For practical purposes, a photocatalyst should be active over several runs. We have tested the photocatalytic activity of **G1.0/450** over five consecutive tests, and this proved to be fully re-usable, see Fig. 6.

Photocatalytic de-NO_x results using the visible white LED lamp are shown in Figure S9. Specimens showed themselves to be

Table 2
Apparent optical E_g, estimated according to the Tauc procedure and the differential reflectance method (dR/dλ).

Sample	Apparent optical E_g									
	Tauc plot†				dR/dλ					
	direct		indirect		anatase		rutile		brookite	
	eV	nm	eV	nm	eV	nm	eV	nm	eV	nm
Ti250/8h	3.25	382	3.00	414	3.28	378	3.16	392	3.41	363
G0.5/250	3.22	385	2.96	418	3.23	384	–	–	–	–
G1.0/250	3.24	382	2.95	421	3.22	384	–	–	–	–
Ti450	3.12	398	2.93	423	3.30	376	3.07	404	3.41	364
G0.5/450	3.15	394	2.92	424	3.32	373	3.08	403	–	–
G1.0/450	3.15	393	2.90	428	3.34	372	3.13	397	–	–

† The absolute error in the Tauc-plot measurements was < 1%.

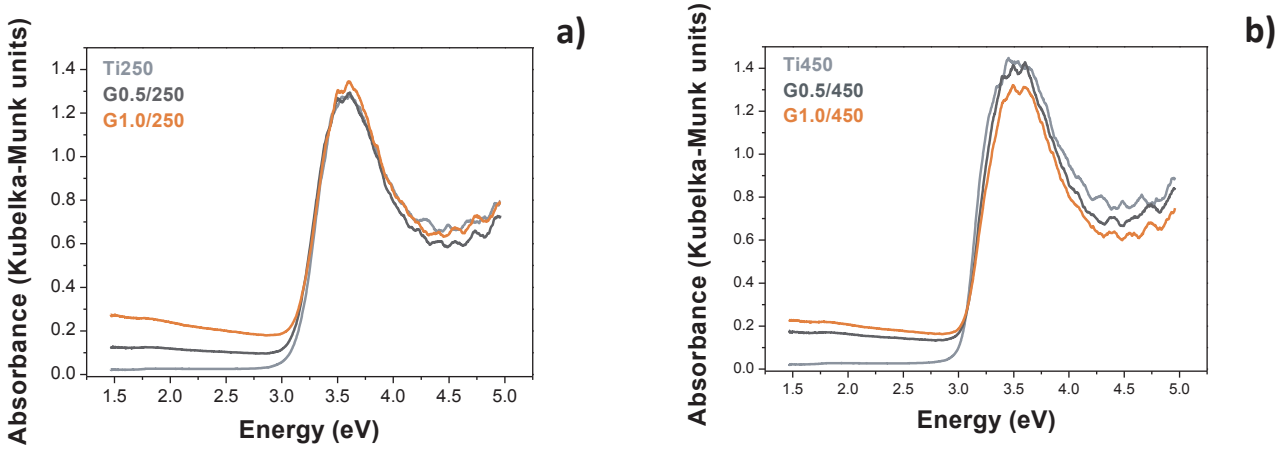

Fig. 3. Optical spectra (pseudo-absorption *versus* energy), as derived by Kubelka – Munk analysis of the DR spectra. a) Specimens thermally treated at 250 °C / 8 h; b) specimens thermally treated at 450 °C / 2 h.

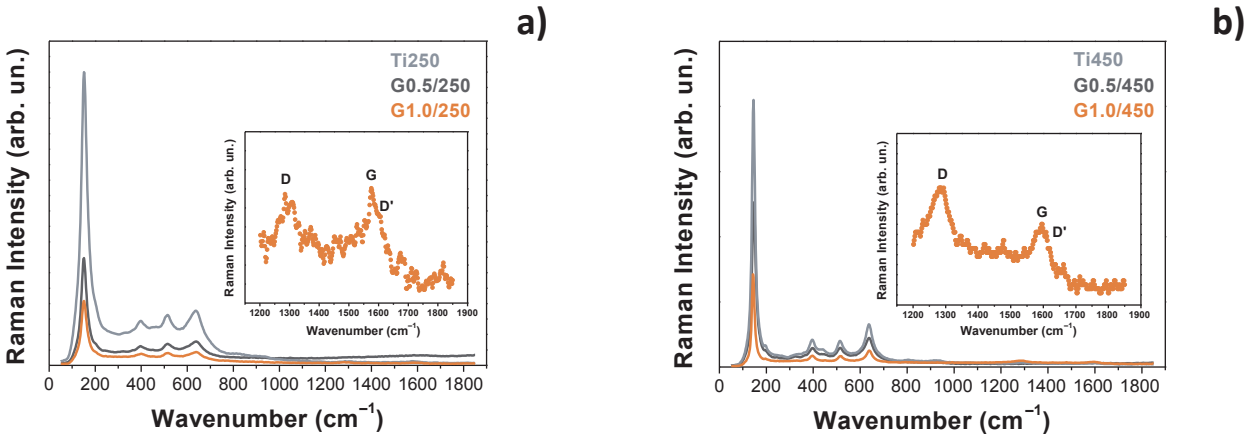

Fig. 4. Raman spectra: a) specimens thermally treated at 250 °C / 8 h; b) specimens thermally treated at 450 °C / 2 h. Insets in a) and b) show the magnified wavenumber region 1200–1850 cm^{-1}, in specimens modified with 1.0 wt% graphene, to highlight the major graphene bands, *D* (~1,300 cm^{-1}), *D′* (around 1,610 cm^{-1}), and *G* (approximately at 1,580 cm^{-1}).

photocatalytically active even using a lamp with no UV component – although less active than with the solar lamp. Activity under visible light illumination might be explained by the mineralogical composition of the specimens: they are indeed composed of anatase and rutile TiO_2 polymorphs (see Table S1). Anatase and rutile nanoparticles when in form of a heterojunction are capable of absorbing visible light, and thus enable photocatalytic activity under visible light illumination [40].

4.2. VOCs removal

4.2.1. Benzene removal

Solar photocatalytic benzene removal results are reported in Fig. 7a,b. These are shown as histograms showing FQEs over a total of 5 h irradiation time, and the first 60 min of reaction pseudo-first order kinetic constants. These data are pretty much comparable with those

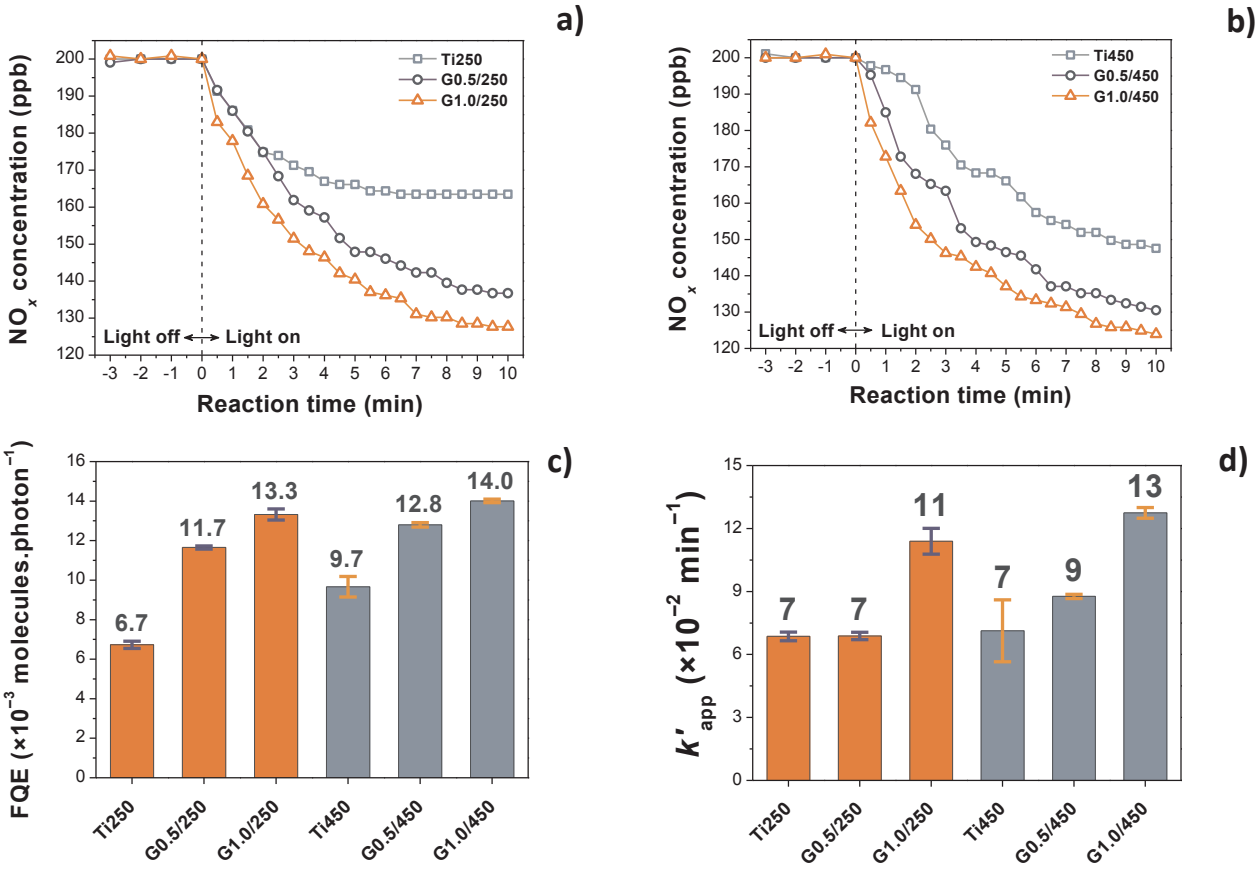

Fig. 5. Photocatalytic de-NO_x plots of the samples irradiated with solar lamp. a) Specimens thermally treated at 250 °C / 8 h; b) specimens thermally treated at 450 °C /2h. In a) and b) the initial negative time zone indicates a period of stabilisation of the chamber; positive time indicates that the light has been turned on starting the experiment. c) Histograms depicting FQEs of prepared photocatalysts for NO_x removal, for a total reaction time of 10 min. d) Histograms showing the first 2 min of reaction pseudo-first order kinetic constants, k'_{app}. Reported values are averaged over three consecutive photocatalytic de-NO_x tests. The error bars represent the standard error over three photocatalytic experiments.

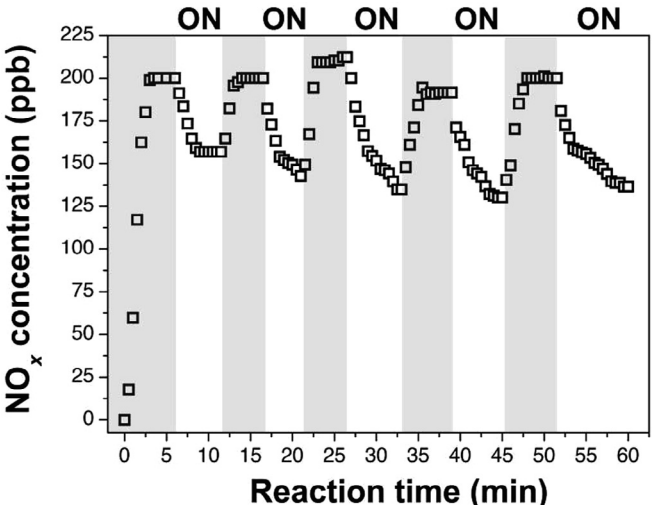

Fig. 6. Solar photocatalytic de-NO_x tests (**G1.0/450**) repeated for five consecutive times. The grey shaded areas represent the time in which the solar lamp was turned off; the white ones the time in which the solar lamp was turned on.

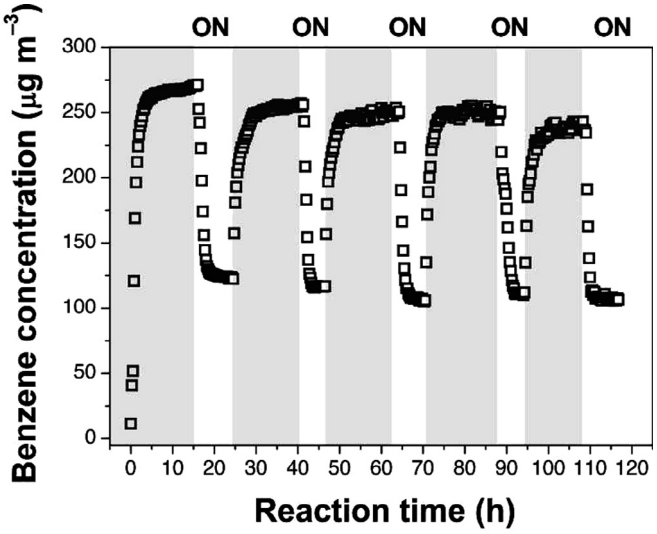

Fig. 8. Photocatalytic benzene removal tests (**G1.0/450**) repeated for five consecutive times. The grey shaded areas represent the time in which the solar lamp was tuned off; the white ones the time in which the solar lamp was turned on.

obtained with the abatement of nitrogen oxides. That is: all of the samples are photocatalytically active; besides, hybridisation of titania with graphene boosted TiO_2 photocatalytic activity. This was approximately two-fold higher for specimens thermally treated at 250 °C / 8 h, the overall FQEs values being: 5.4 × 10^{-8}, 10.3 × 10^{-8}, and 10.0 × 10^{-8} molecules.photon^{-1} in **Ti250**, **G0.5/250**, and **G1.0/250**, respectively, *cf* Fig. 7a. Increased thermal treatment, led to higher overall FQEs rates: 7.9 × 10^{-8}, 10.1 × 10^{-8}, and 11.0 × 10^{-8} molecules.photon^{-1} in **Ti450**, **G0.5/450**, and **G1.0/450**, over 5 h irradiation time. However, taking into consideration the initial 60 min of benzene removal, Fig. 7b, specimens with 1.0 wt% graphene had a photocatalytic activity that was 3 times higher than that of unmodified titania in the set of specimens thermally treated at 250 °C / 8 h – k'_{app} values of **Ti250** (**G1.0/250**) were: 16 × $10^{-2}h^{-1}$ (49 × $10^{-2}h^{-1}$). In case of specimens thermally treated at 450 °C / 2 h, the k'_{app} values of **Ti450** and **G1.0/450** were 20 × $10^{-2}h^{-1}$ and 53 × $10^{-2}h^{-1}$, respectively – more than two times higher. Like the de-NO_x tests, **G1.0/450** proved itself to be extremely repeatable also in consecutive photocatalytic benzene removal experiments, as depicted in Fig. 8.

Visible-light photocatalytic benzene removal results are displayed in Figure S10. Unlike de-NO_x abatement, graphene addition did not increase the visible-light photocatalytic activity of titania in the removal of benzene.

4.2.2. Isopropanol oxidation

UV–Vis photocatalytic activity results of the samples against the removal of IPA, shown as FQE and formation rates of acetone (ppm.h^{-1}), are summarised in Fig. 9a,b. Consistent with the data obtained with the NO_x abatement and benzene removal (*cf* *Section 4.1*, and *Section 4.2.1*), addition of graphene to TiO_2 aided the photocatalytic assisted IPA oxidation. This is shown by FQEs values (Fig. 9a): pure TiO_2 at 250 °C / 8 h (**Ti250**) showed an FQE acetone formation rate of 1.8 × 10^{-2} molecules.photon^{-1}. Upon hybridisation with 0.5 and 1.0 wt% graphene, the FQE acetone formation rate increased to 2.9 and 2.6 × 10^{-2} molecules.photon^{-1} (**G0.5/250** and **G1.0/250**, Fig. 9a). This is also displayed by acetone formation rates of 210, 330, and 295 ppm.h^{-1} for **Ti250**, **G0.5/250** and **G1.0/250**, respectively, Fig. 9b).

At the higher thermal treatment, addition of 0.5 and 1.0 wt% graphene resulted in acetone formation rate (in terms of FQE) more than the double than that of TiO_2: 2.2 × 10^{-2}, 4.4 × 10^{-2}, and 4.8 × 10^{-2}

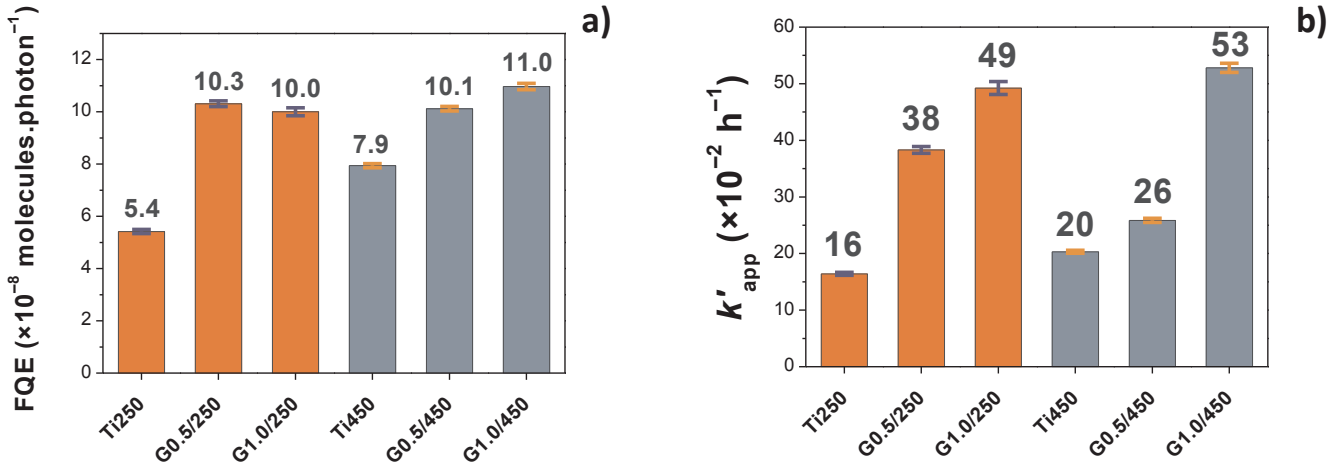

Fig. 7. a) Histograms depicting the FQE rates of prepared photocatalysts for benzene removal using the solar lamp, for a total reaction time of 5 h. b) Histograms showing the pseudo-first order kinetic constants (first 1 h reaction), k'_{app} (solar lamp). Reported values are averaged over three consecutive photocatalytic benzene removal tests. The error bars represent the standard error over three photocatalytic experiments.

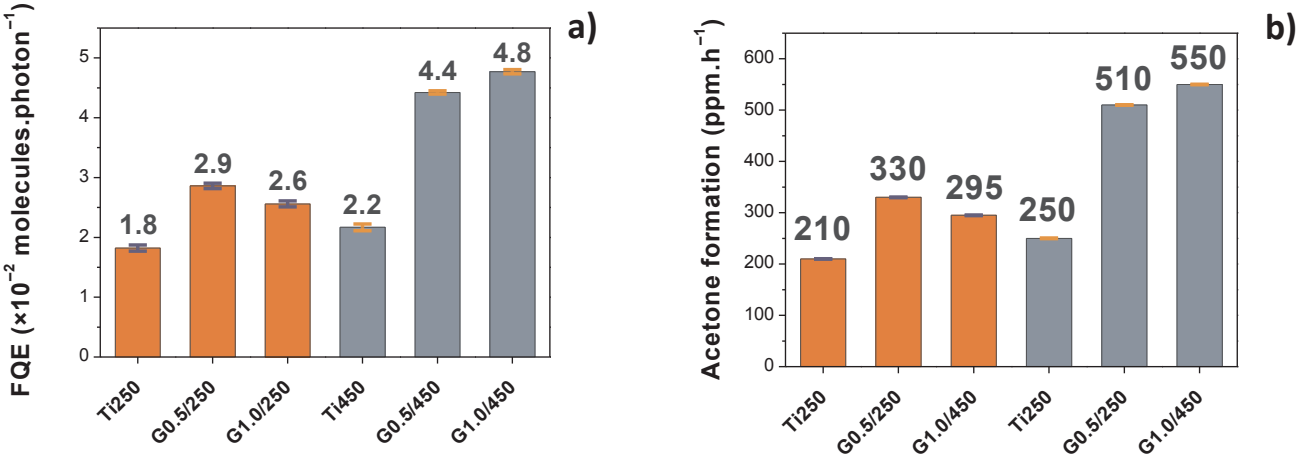

Fig. 9. Photocatalytic isopropanol degradation under UV–Vis light exposure, expressed as: a) FQEs of initial acetone formation; b) rate constant of the initial acetone formation. In a) and b), the total irradiation time was set at 1 h. The error bars represent the standard error over three photocatalytic experiments.

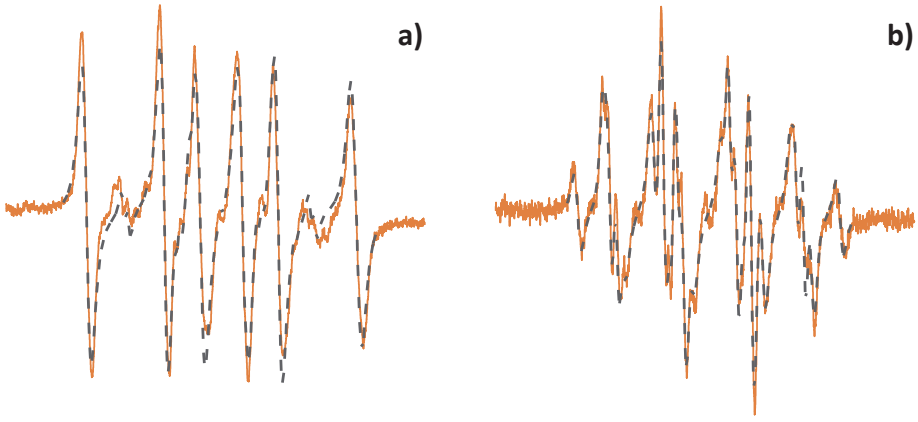

Fig. 10. Experimental (orange solid line) and simulated (blue dashed line) EPR spectra (magnetic field sweep width 8.0 mT) of: (a) IPA, and (b) benzene **G1.0/450** impregnated powders in the presence of DMPO spin trapping agent upon LED@365 nm exposure (dose 4.5 J.cm^{-2}). The concentration of oxygen was reduced by the slight stream of argon before exposure. (For interpretation of the references to colour in this figure legend, the reader is referred to the web version of this article.)

molecules.photon^{-1} acetone FQE rate for **Ti450**, **G0.5/450**, and **G1.0/450**, respectively, *cf* Fig. 9a. This correlated well with acetone formation rates values of: 250, 510, and 550 ppm.h^{-1}, respectively (Fig. 9b).

Contrasting results occurred when visible-light radiation was used, *cf* Figure S11. At 250 °C, acetone formation rates decreased with the increase of graphene in the system (*i.e.*, the photocatalytic activity was: **G1.0/250** < **G0.5/250** < **Ti250**). On the contrary, when the specimens were thermally treated at 450 °C / 2 h, IPA oxidation had this trend: **G1.0/450** > **G0.5/450** > **Ti450**, even though the rise in photocatalytic activity was little (18, 15, and 14 ppm.h^{-1}, respectively).

Therefore, results reported here emphasise once again the extreme complexity of photocatalytic air purification processes (using different molecules as pollutant to be removed and different light sources).

4.3. EPR spin trapping technique

The EPR spin trapping technique was applied for the detection of transient paramagnetic species formed upon UV-A exposure of powdered photocatalysts impregnated with benzene or IPA containing DMPO spin trap. The analogous DMPO spin-adducts were detected for the photocatalytic systems prepared with **Ti450** and **G0.5/450** in the presence of IPA or benzene. Fig. 10 represents the experimental EPR spectra obtained upon continuous UV-A exposure of the powdered photocatalyst **G1.0/450** impregnated with IPA/DMPO or benzene/DMPO, along with their simulations. The UV-A photoactivation of **G1.0/450**/IPA/DMPO resulted in the generation of superimposed signals corresponding to the simultaneous production of various DMPO-adducts. The asymmetric six-line signal represents the spin-adducts of two carbon-centred radicals with slightly different spin-Hamiltonian parameters, *i.e.* $^{\bullet}$DMPO-CR$_1$ (a_N = 1.453 mT, a_H^{β} = 2.178 mT, g = 2.0057) and $^{\bullet}$DMPO-CR$_2$ (a_N = 1.527 mT, a_H^{β} = 2.185 mT, g = 2.0057) that dominates the EPR spectrum (Fig. 10a). Additionally, the spin-adduct of oxygen-centred radical (a_N = 1.287 mT, a_H^{β} = 0.999 mT, a_H^{γ} = 0.098 mT, g = 2.0057) was detected as minor spectral component, and was attributed to the trapped $O_2^{\bullet-}$/$HO_2^{\bullet}$ radical generated *via* interaction of photoelectrons with O_2 [76]. The formation of oxygen- and carbon-centred radicals detected as the corresponding DMPO-adducts is well compatible with the oxidation of IPA adsorbed on TiO_2 surface. The photocatalytic oxidative transformation of IPA is a complex process and acetone as intermediate may be formed by several reaction pathways [77,78]. Under those experimental conditions, IPA molecules adsorbed on the photocatalysts' surface reacts with the photogenerated holes forming the primary alkoxy radicals $(CH_3)_2CHO^{\bullet}$. These species rapidly react with other IPA molecules and/or with hydroxyl radicals producing hydroxyalkyl radical $[(CH_3)_2{}^{\bullet}C(OH)]$, transformed *via* consecutive reactions to acetone [77,78].

Upon continuous LED@365 nm exposure of **G1.0/450**/benzene/DMPO, the signals of oxygen-centred spin-adducts dominate the EPR spectrum (Fig. 10b). The crucial twelve-line signal was attributed to the superoxide radical anion added on the DMPO molecule ($^{\bullet}$DMPO-O_2^{-}/O_2H, spin-Hamiltonian parameters a_N = 1.279 mT, a_H^{β} = 1.012 mT, a_H^{γ} = 0.139 mT, g = 2.0061). The simulation analysis of the complex experimental EPR spectrum revealed the presence of DMPO-adducts with carbon-centred and alkoxy radicals, originating from benzene molecule [79]. The photocatalytic oxidation of benzene on titania surface is a very complex process including photogenerated holes,

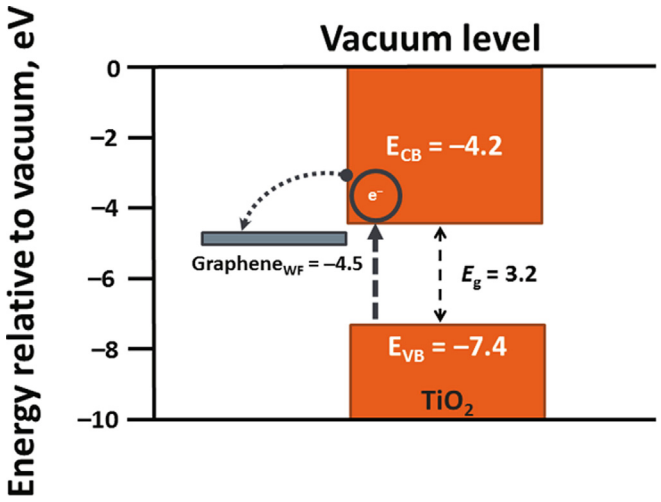

Fig. 11. Proposed mechanism for improved spatial charge carrier separation in a graphene-TiO_2 hybrid material (following to UV–Vis excitation). In the band diagram, relative to the absolute vacuum scale, the dashed yellow arrow shows the electron transferring in titania (from the valence band to the conduction band) due to photocatalysis; the dotted yellow arrow depicts the successive electron transferring from the conduction band of TiO_2 to graphene. Energy levels of TiO_2 are from specimen **G1.0/450** – estimated assuming a direct E_g model, and considering the absolute electronegativity values of the constituent atoms of the material [82,83]. The value for the working function (WF) of graphene is from Liang and Ang [84]. (For interpretation of the references to colour in this figure legend, the reader is referred to the web version of this article.)

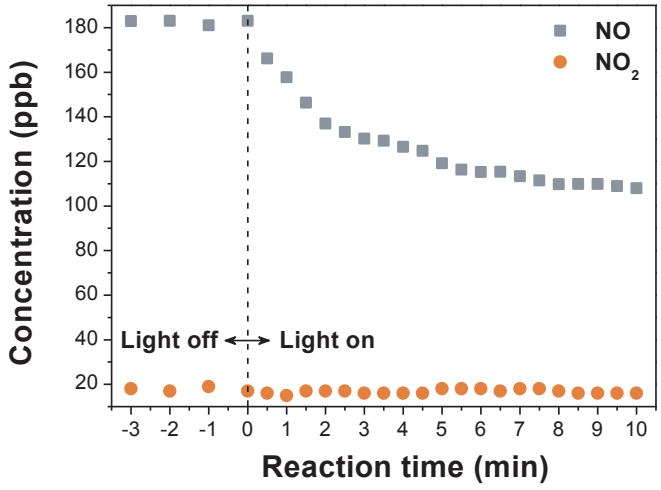

Fig. 12. Concentration of NO and NO_2 *versus* reaction time in **G1.0/450**.

electrons and reactive oxygen species [80,81]. The photogenerated holes may interact with benzene molecule forming benzene radical cation. However, in the presence of HO^-/H_2O adsorbed on photocatalysts' surface, the holes effectively react with HO^-/H_2O producing hydroxyl radicals. The addition of $HO^{\bullet}$ to benzene molecule leads to the formation of hydroxy cyclohexadienyl radical, which can enter in consecutive reactions with oxygen, benzene or other species. The photogenerated electrons react with molecular oxygen forming superoxide radical anions. The benzene radical cation may interact also with both $O_2^{\bullet-}$ and O_2 and *via* transient benzene peroxy radicals, and phenol is formed. The DMPO spin-adducts of peroxy radicals are not stable and may rapidly disproportionate to the detected alkoxy-radical adducts. Alternatively, benzene-based alkoxy radicals formed by the transformation of benzene peroxy radicals, can be directly trapped by DMPO.

4.4. Mechanistic insight of the photocatalytic activity

Typically, in a photocatalytic process, the following reactions happen at the surface of a semiconductor material:

$$TiO_2/graphene + h\nu \rightarrow e_{CB}^- - + h_{VB}^+ \quad (1)$$

$$h_{VB}^+ + H_2O_{(ads)} \rightarrow HO^{\cdot}_{(ads)} + H^+ \quad (2)$$

$$e_{CB}^- - + O_{2(ads)} \rightarrow O_{2(ads)}^{\cdot-} \quad (3)$$

$$e_{CB}^- - + h_{VB}^+ \rightarrow energy \quad (4)$$

It has been shown that graphene addition improves the electron transport in TiO_2/graphene hybrid materials [31], therefore being a support with an added-value for TiO_2 based photocatalytic reactions. The photogenerated electrons, from the TiO_2 component, are swiftly transferred to the surrounding graphene sheets. Graphene sheets behave as a highway for the mobility of such electrons, allowing for an increase in the separation of the photogenerated exciton [37]. This is schematically drawn in Fig. 11.

Those electrons are then involved in reductive reactions, *i.e.* the formation of active superoxide ion ($O_2^{\bullet-}$) species with oxygen from the environment (equation (3)).

According to what is reported above, *Section 4.3*, and looking at Fig. 12, it is reasonable assuming NO_x abatement to mainly follow the NO oxidation path by $O_2^{\bullet-}$ species [85]:

$$NO + O_{2(ads)}^{\cdot-} \rightarrow NO_3^- - \quad (5)$$

$$NO_3^- - + H^+ \rightarrow HNO_3 \quad (6)$$

It has been proposed that the de-NO_x cycle shall be ideally closed by HNO_3 removal *via* water treatment from the photocatalyst surface [Equation (7)] [86]:

$$HNO_{3(ads)} \rightarrow HNO_{3(aq)} \quad (7)$$

In the plot displaying the concentration of NO and NO_2 *versus* reaction time (Fig. 12), we observe the (photocatalytic) abatement of NO, whilst the concentration of NO_2 is virtually stable over the time. The final product of NO_x abatement is HNO_3, which can be easily eluted from the catalyst into water [Equation (7)] [87].

A similar hypothesis can be made for IPA degradation. Indeed, Palmisano and colleagues proposed the photocatalytic oxidation of IPA to acetone to follow this path [88]:

$$(CH_3)_2CHOH + O_{2(ads)}^{\cdot-} \rightarrow (CH_3)_2CO + H_2O + e^- - \quad (8)$$

$$(CH_3)_2CHOH + HO^{\cdot}_{(ads)} \rightarrow (CH_3)_2HCO^{\cdot} + H_2O \quad (9)$$

$$(CH_3)_2HCO^{\cdot} \rightarrow (CH_3)_2CO + H^+ + e^- - \quad (10)$$

The EPR spin trapping technique indeed showed the effective generation of carbon-centred radicals upon exposure, supporting the proposed mechanism.

However, photocatalytic removal of hydrocarbons can be a much more complicated issue. It has been found by Rickard and colleagues that a complete isoprene (C_5H_8) atmospheric oxidation involved 1,926 different degradation steps, together with the formation of 602 unique intermediate organic species before CO_2 and water were eventually formed [89]. Therefore, recognising (qualitatively and quantitatively) all of the intermediated of benzene photocatalytic oxidation is beyond the scope of this work. However, with the available experimental data together with the aid of previous literature, we can speculate about (some of) the degradation products of benzene. The generation of transient radical intermediates upon exposure responsible for the degradation processes of the benzene molecule was confirmed by EPR spin trapping technique. In Fig. 13 are reported the gas-chromatograms as extracted (at selected irradiation times) from the gas-analyser during the photocatalytic experiments – specimen **G1.0/450**. At time zero, just before switching the solar lamp on, benzene is virtually the only

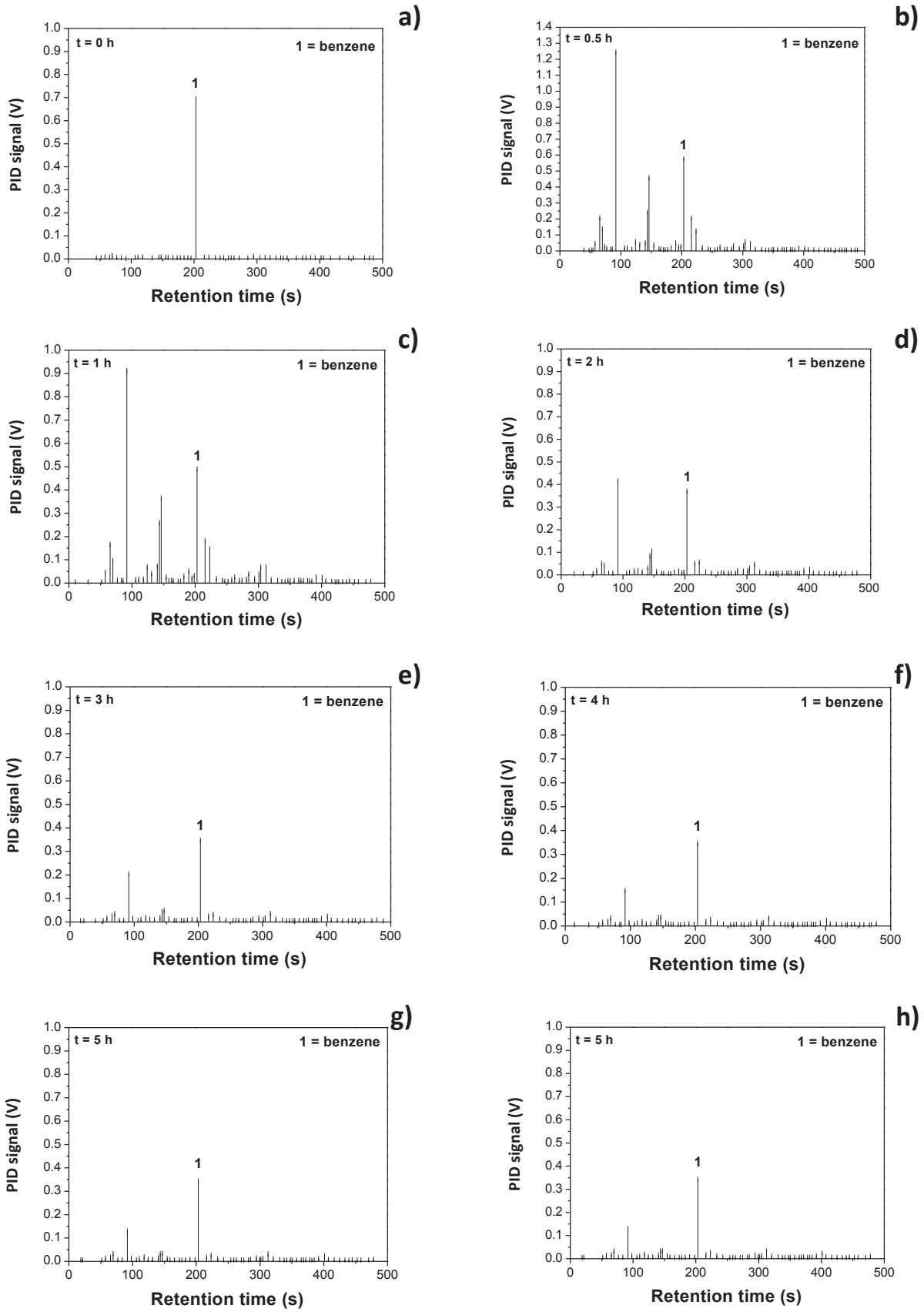

Fig. 13. G1.0/450 gas-chromatograms as extracted from the VOC-72 M gas analyser at: a) t = 0; b) t = 0.5 h; c) t = 1 h; d) t = 2 h; e) t = 3 h; f) t = 4 h; g) t = 5 h; h) t = 6 h of solar lamp irradiation time. Benzene (symbol **1** in the gas-chromatograms) is at 202 s retention time.

compound found (Fig. 13a). Lighter and heavier degradation compounds than benzene are detected just after 0.5 h of solar irradiation, together with a decrease in benzene concentration, Fig. 13b. Phenol (molar mass, M = 94.11 g.mol^{-1}), 1,4-benzoquinone (M = 108.095 g.mol^{-1}), hydroquinone (M = 110.11 g.mol^{-1}), and benzoic acid (M = 122.12 g.mol^{-1}) were detected by means of GC/MS and DRIFT techniques as photocatalytic benzene removal by-products [90,91,80,92]. Those compounds all have a higher molar mass than benzene (M = 78.11 g.mol^{-1}), therefore their presence is reasonable. Ollis and co-authors also found carboxylic acids – acetic and formic acid (M = 60.052, and 46.03 g.mol^{-1}, respectively) – as intermediates of benzene oxidation [91]. The amounts of benzene and its degradation compound gradually decrease as the exposure time increases (Fig. 13c,d). Eventually, after 3 h irradiation time and ongoing (Fig. 13e-h), chromatograms virtually report only benzene and lighter degradation compounds of it. Therefore, from these results, VOCs should not be treated as a single pollutant [93]. Besides, we can postulate that, as proposed by Lichtin and Sadeghi [94], the formation of those intermediates might delay/inhibit the reaction(s) responsible for benzene's mineralisation, therefore competing with benzene, and themselves, in the photocatalytic reaction, hampering the overall kinetic of benzene removal. TiO_2 gas-phase photocatalytic oxidation of benzene confirms to be a complex matter, having different reaction mechanisms and pathways under different reaction conditions [81]. Those pollutants (*i.e.* nitrogen oxides and VOCs) might be found mixed together in a real outdoor environment. At this aim, a study by Chan and co-authors showed that the presence of NO promoted the photodegradation of mixed VOCs (BTEX) over Evonik Aeroxide TiO_2 P25 under low humidity level; *vice versa*, the presence of BTEX reduced the conversion of NO, and the generation of NO_2 [95].

5. Conclusions

Air pollution is a cause of adverse health effects worldwide, therefore has to be treated as a global problem. To (partly) tackle this concern, we have synthesised, *via* a green, clean, and simple sol–gel method, titania/graphene (0.5 and 1.0 wt% graphene) hybrid nanomaterials. Photocatalytic activity of as-prepared materials was tested against three major pollutants found outdoor: nitrogen oxides (*i.e.* NO + NO_2), and two different kinds of volatile organic compounds, namely: benzene and isopropanol. EPR spin trapping technique proved that, upon UV-A irradiation, distinct radicals were formed in presence of isopropanol and benzene, thus leading to different yet complex reaction pathways. Results showed that the addition of 1.0 wt% of graphene to TiO_2 enabled (at least) a two-fold increase in the photocatalytic removal of those gaseous pollutants, being fully recyclable over repeated tests – thus showing the stability of that system during the oxidising working conditions of photocatalytic reactions. Indeed, the addition of graphene to that semiconducting material acted as a *highway* for the electron mobility, enhancing the separation of the photogenerated exciton, decreasing their recombination rate. This makes our material an ideal candidate for multi-purpose environmental applications.

Declaration of Competing Interest

The authors declare that they have no known competing financial interests or personal relationships that could have appeared to influence the work reported in this paper.

Acknowledgements

This work was partly developed within the scope of the bilateral project between Portugal and the Slovak Republic, FCT/484/15/01/2019/S and in the frame of the project CICECO-Aveiro Institute of Materials, UIDB/50011/2020 & UIDP/50011/2020, financed by national funds through the Portuguese Foundation for Science and Technology/MCTES. This study was also financially supported by Scientific Grant Agency of the Slovak Republic (VEGA Project 1/0026/18) and Slovak Research and Development Agency under the contract No. SK-PT-2018-0007. David Maria Tobaldi is overly grateful to FCT and to Portuguese national funds (OE), through FCT, I.P., in the scope of the framework contract foreseen in the numbers 4, 5 and 6 of the article 23, of the Decree-Law 57/2016, of August 29, changed by Law 57/2017, of July 19. This project has also received partial funding from the European Union's Horizon 2020 research and innovation programme under grant agreement No 823717 – ESTEEM3. Luc Lajaunie gratefully acknowledges the support from the Spanish *Ministerio de Economia y Competitividad* (PID2019-107578GA-I00). Authors wish to thank the European Structural and Investment Funds in the FEDER component, through the Operational Programme for Competitiveness and Internationalization (COMPETE 2020) under the Project GNESIS – Graphenest's New Engineered System and its Implementation Solutions – Funding Reference: POCI-01-0247-FEDER-033566, European Regional Development Fund. Nejc Rozman and Andrijana Sever Škapin acknowledge the financial support provided by the Slovenian Research Agency (grant No. NC-0002 and No. P2-0273), and Slovenian Ministry of Education, Science and Sport for funding through the "*Promotion of the employment of young PhDs*" program. We are very much obliged to Miss Dafne Maria Glaglanon for proof-editing the English of the manuscript.

Appendix A. Supplementary data

Supplementary data to this article can be found online at https://doi.org/10.1016/j.cej.2020.126651.

References

[1] WHO, Air pollution, (2019). https://www.afro.who.int/health-topics/air-pollution.
[2] J.H. Seinfeld, S.N. Pandis, Atmospheric chemistry and physics: from air pollution to climate change, 3rd edition, Wiley, Hoboken, New Jersey, 2016.
[3] IARC Working Group on the Evaluation of Carcinogenic Risks to Humans, International Agency for Research on Cancer, Outdoor air pollution, 2016. http://www.ncbi.nlm.nih.gov/books/NBK368024.
[4] B.C. McDonald, J.A. de Gouw, J.B. Gilman, S.H. Jathar, A. Akherati, C.D. Cappa, J.L. Jimenez, J. Lee-Taylor, P.L. Hayes, S.A. McKeen, Y.Y. Cui, S.-W. Kim, D.R. Gentner, G. Isaacman-VanWertz, A.H. Goldstein, R.A. Harley, G.J. Frost, J.M. Roberts, T.B. Ryerson, M. Trainer, Volatile chemical products emerging as largest petrochemical source of urban organic emissions, Science 359 (6377) (2018) 760–764.
[5] D. Campbell-Lendrum, A. Prüss-Ustün, Climate change, air pollution and noncommunicable diseases, Bull. World Health Organ. 97 (2) (2019) 160–161.
[6] EPA, Particulate Matter (PM) Basics, (2019). https://www.epa.gov/pm-pollution/particulate-matter-pm-basics.
[7] J. Ângelo, L. Andrade, L.M. Madeira, A. Mendes, An overview of photocatalysis phenomena applied to NOx abatement, J. Environ. Manage. 129 (2013) 522–539.
[8] C. Guerreiro, A. González Ortiz, F. de Leeuw, M. Viana, A. Colette, European Environment Agency, Air quality in Europe - 2018 report, 2018. https://data.europa.eu/doi/10.2800/777411.
[9] M.C. Collivignarelli, A. Abbà, G. Bertanza, R. Pedrazzani, P. Ricciardi, M. Carnevale Miino, Lockdown for CoViD-2019 in Milan: What are the effects on air quality? Sci. Total Environ. 732 (2020) 139280, https://doi.org/10.1016/j.scitotenv.2020.139280.
[10] W.H. Organization (Ed.), Air quality guidelines for Europe, 2nd ed, World Health Organization, Regional Office for Europe, Copenhagen, 2000.
[11] L. Benbrahim-Tallaa, R.A. Baan, Y. Grosse, B. Lauby-Secretan, F. El Ghissassi, V. Bouvard, N. Guha, D. Loomis, K. Straif, Carcinogenicity of diesel-engine and gasoline-engine exhausts and some nitroarenes, Lancet Oncol. 13 (7) (2012) 663–664.
[12] Volatile Organic Compounds (2019).
[13] A.H. Goldstein, I.E. Galbally, Known and Unexplored Organic Constituents in the Earth's Atmosphere, Environ. Sci. Technol. 41 (5) (2007) 1514–1521.
[14] R. Atkinson, Atmospheric chemistry of VOCs and NO_x, Atmos. Environ. 34 (2000) 2063–2101, https://doi.org/10.1016/S1352-2310(99)00460-4.
[15] M.J. Muñoz-Batista, U. Caudillo-Flores, F. Ung-Medina, M.a. del Carmen Chávez-Parga, J.A. Cortés, A. Kubacka, M. Fernández-García, Gas phase 2-propanol degradation using titania photocatalysts: Study of the quantum efficiency, Appl. Catal. B 201 (2017) 400–410.
[16] R.J. Slaughter, R.W. Mason, D.M.G. Beasley, J.A. Vale, L.J. Schep, Isopropanol

poisoning, Clinical Toxicology 52 (5) (2014) 470–478.
[17] W.R.O. for Europe, WHO Guidelines for Indoor Air Quality: Selected Pollutants., World Health Organization, Geneva, 2010. https://public.ebookcentral.proquest.com/choice/publicfullrecord.aspx?p=1582967.
[18] R. Snyder, C.C. Hedli, An Overview of Benzene Metabolism, Environ. Health Perspect. 104 (1996) 1165, https://doi.org/10.2307/3433158.
[19] D. Spasiano, R. Marotta, S. Malato, P. Fernandez-Ibañez, I. Di Somma, Solar photocatalysis: Materials, reactors, some commercial, and pre-industrialized applications. A comprehensive approach, Appl. Catal. B 170-171 (2015) 90–123.
[20] S.E. Braslavsky, A.M. Braun, A.E. Cassano, A.V. Emeline, M.I. Litter, L. Palmisano, V.N. Parmon, N. Serpone, Glossary of terms used in photocatalysis and radiation catalysis (IUPAC Recommendations 2011), Pure and Applied Chemistry. 83 (2011). https://doi.org/10.1351/PAC-REC-09-09-36.
[21] A. Fujishima, K. Hashimoto, T. Watanabe, TiO2 photocatalysis: fundamentals and applications, BKC, Tokyo, Japan, 1999.
[22] R. Qian, H. Zong, J. Schneider, G. Zhou, T. Zhao, Y. Li, J. Yang, D.W. Bahnemann, J.H. Pan, Charge carrier trapping, recombination and transfer during TiO_2 photocatalysis: An overview, Catal. Today 335 (2019) 78–90.
[23] O. Ola, M.M. Maroto-Valer, Review of material design and reactor engineering on TiO_2 photocatalysis for CO2 reduction, J. Photochem. Photobiol., C 24 (2015) 16–42.
[24] K.S. Novoselov, A.K. Geim, I.V. Morozov, D. Jiang, Y. Zhang, Y, S.V. Dubonos, I.V. Grigorieva, A.A. Firsov, Electric Field Effect in Atomically Thin Carbon Films, Science. 306 (2004) 666–669. https://doi.org/10.1126/science.1102896.
[25] A.K. Geim, K.S. Novoselov, The rise of graphene, Nature Mater 6 (3) (2007) 183–191.
[26] Ol. Bubnova, The graphene times, Nat. Nanotechnol. 14 (2019) 903–903. https://doi.org/10.1038/s41565-019-0561-4.
[27] Nan Zhang, Min-Quan Yang, Siqi Liu, Yugang Sun, Yi-Jun Xu, Waltzing with the Versatile Platform of Graphene to Synthesize Composite Photocatalysts, Chem. Rev. 115 (18) (2015) 10307–10377.
[28] Quanjun Xiang, Bei Cheng, Jiaguo Yu, Graphene-Based Photocatalysts for Solar-Fuel Generation, Angew. Chem. Int. Ed. 54 (39) (2015) 11350–11366.
[29] Rowan Leary, Aidan Westwood, Carbonaceous nanomaterials for the enhancement of TiO2 photocatalysis, Carbon 49 (3) (2011) 741–772.
[30] Quanjun Xiang, Jiaguo Yu, Mietek Jaroniec, Graphene-based semiconductor photocatalysts, Chem. Soc. Rev. 41 (2) (2012) 782–796.
[31] Xin Li, Jiaguo Yu, S. Wageh, Ahmed A. Al-Ghamdi, Jun Xie, Graphene in Photocatalysis: A Review, Small 12 (48) (2016) 6640–6696.
[32] Marisol Faraldos, Ana Bahamonde, Environmental applications of titania-graphene photocatalysts, Catal. Today 285 (2017) 13–28.
[33] P. Fernández-Ibáñez, M.I. Polo-López, S. Malato, S. Wadhwa, J.W.J. Hamilton, P.S.M. Dunlop, R. D'Sa, E. Magee, K. O'Shea, D.D. Dionysiou, J.A. Byrne, Solar photocatalytic disinfection of water using titanium dioxide graphene composites, Chem. Eng. J. 261 (2015) 36–44.
[34] Ewelina Kusiak-Nejman, Antoni W. Morawski, TiO_2/graphene-based nanocomposites for water treatment: A brief overview of charge carrier transfer, antimicrobial and photocatalytic performance, Appl. Catal. B 253 (2019) 179–186.
[35] He Guo, Nan Jiang, Huijuan Wang, Kefeng Shang, Na Lu, Jie Li, Yan Wu, Enhanced catalytic performance of graphene-TiO_2 nanocomposites for synergetic degradation of fluoroquinolone antibiotic in pulsed discharge plasma system, Appl. Catal. B 248 (2019) 552–566.
[36] Kannappan Panchamoorthy Gopinath, Nagarajan Vikas Madhav, Abhishek Krishnan, Rajagopal Malolan, Goutham Rangarajan, Present applications of titanium dioxide for the photocatalytic removal of pollutants from water: A review, J. Environ. Manage. 270 (2020) 110906, https://doi.org/10.1016/j.jenvman.2020.110906.
[37] A. Trapalis, N. Todorova, T. Giannakopoulou, N. Boukos, T. Speliotis, D. Dimotikali, Jiaguo Yu, TiO2/graphene composite photocatalysts for NO_x removal: A comparison of surfactant-stabilized graphene and reduced graphene oxide, Appl. Catal. B 180 (2016) 637–647.
[38] Wenguang Wang, Jiaguo Yu, Quanjun Xiang, Bei Cheng, Enhanced photocatalytic activity of hierarchical macro/mesoporous TiO_2–graphene composites for photodegradation of acetone in air, Appl. Catal. B 119-120 (2012) 109–116.
[39] Mariana R.F. Silva, Mirtha A.O. Lourenço, David Maria Tobaldi, Carla F. da Silva, Maria Paula Seabra, Paula Ferreira, Carbon-modified titanium oxide materials for photocatalytic water and air decontamination, Chem. Eng. J. 387 (2020) 124099, https://doi.org/10.1016/j.cej.2020.124099.
[40] D.M. Tobaldi, L. Lajaunie, N. Rozman, A.P.F. Caetano, M.P. Seabra, A. Sever Škapin, R. Arenal, J.A. Labrincha, Impact of the absolute rutile fraction on TiO_2 visible-light absorption and visible-light-promoted photocatalytic activity, J. Photochem. Photobiol., A 382 (2019) 111940, https://doi.org/10.1016/j.jphotochem.2019.111940.
[41] A.C. Larson, R.B. Von Dreele, General Structure Analysis System (GSAS), Los Alamos National Laboratory Report LAUR (2004).
[42] Brian H. Toby, EXPGUI , a graphical user interface for GSAS, J Appl Crystallogr 34 (2) (2001) 210–213.
[43] P. Scardi, M. Leoni, Whole powder pattern modelling, Acta Crystallogr A Found Crystallogr 58 (2) (2002) 190–200.
[44] M. Leoni, T. Confente, P. Scardi, PM2K: a flexible program implementing Whole Powder Pattern Modelling, Z. Kristallogr. Suppl. 2006 (suppl_23_2006) (2006) 249–254.
[45] P. Stadelmann, JEMS-SAAS, (2014).
[46] Takashi Sato, Yuzo Hamada, Masaru Sumikawa, Sadao Araki, Hideki Yamamoto, Solubility of Oxygen in Organic Solvents and Calculation of the Hansen Solubility Parameters of Oxygen, Ind. Eng. Chem. Res. 53 (49) (2014) 19331–19337.
[47] Stefan Stoll, Arthur Schweiger, EasySpin, a comprehensive software package for spectral simulation and analysis in EPR, J. Magn. Reson. 178 (1) (2006) 42–55.
[48] D.M. Tobaldi, L. Lajaunie, M. López Haro, R.A.S. Ferreira, M. Leoni, M.P. Seabra, J.J. Calvino, L.D. Carlos, J.A. Labrincha, Synergy of Neodymium and Copper for Fast and Reversible Visible-light Promoted Photochromism, and Photocatalysis, in Cu/Nd-TiO 2 Nanoparticles, ACS Appl. Energy Mater. 2 (5) (2019) 3237–3252.
[49] W.H.O.R.O. for Europe, Air quality guidelines for Europe, (2000). https://apps.who.int/iris/handle/10665/107335.
[50] European Environment Agency, Nitrogen dioxide - Annual limit values for the protection of human health, https://www.eea.europa.eu/data-and-maps/figures/nitrogen-dioxide-annual-limit-values-for-the-protection-of-human-health.
[51] Mohamed Karmaoui, Luc Lajaunie, David Maria Tobaldi, Gianluca Leonardi, Chahinez Benbayer, Raul Arenal, João A. Labrincha, Giovanni Neri, Modification of anatase using noble-metals (Au, Pt, Ag): Toward a nanoheterojunction exhibiting simultaneously photocatalytic activity and plasmonic gas sensing, Appl. Catal. B 218 (2017) 370–384.
[52] Andrea Giampiccolo, David Maria Tobaldi, Salvatore Gianluca Leonardi, Billy James Murdoch, Maria Paula Seabra, Martin P. Ansell, Giovanni Neri, Richard J. Ball, Sol gel graphene/TiO2 nanoparticles for the photocatalytic-assisted sensing and abatement of NO_2, Appl. Catal. B 243 (2019) 183–194.
[53] World Health Organization, WHO. Guidelines for Indoor Air Quality: Selected Pollutants, 2010, WHO - Guidelines for Indoor Air Quality: Selected Pollutants. (2010). www.euro.who.int/_data/assets/pdf_file/0009/128169/e94535.pdf.
[54] Andrew Mills, Stephen Le Hunte, An overview of semiconductor photocatalysis, J. Photochem. Photobiol., A 108 (1) (1997) 1–35.
[55] R.I. Bickley, G. Munuera, F.S. Stone, Photoadsorption and photocatalysis at rutile surfaces: II. Photocatalytic oxidation of isopropanol, J. Catal. 31 (1973) 398–407, https://doi.org/10.1016/0021-9517(73)90311-4.
[56] G. Munuera, F. Moreno, J.A. Prieto, Temperature Programmed Desorption of Water Adsorbed on Anatase Surfaces, Z. Phys. Chem. 78 (3_4) (1972) 113–117.
[57] S.A. Larson, J.A. Widegren, J.L. Falconer, Transient Studies of 2-Propanol Photocatalytic Oxidation on Titania, J. Catal. 157 (2) (1995) 611–625.
[58] S. Obregón, G. Colón, Excellent photocatalytic activity of Yb^{3+}, Er^{3+} co-doped $BiVO_4$ photocatalyst, Appl. Catal. B 152-153 (2014) 328–334.
[59] Huilei Wang, Xiaoyun Gao, Guorong Duan, Xujie Yang, Xiaoheng Liu, Facile preparation of anatase–brookite–rutile mixed-phase N-doped TiO_2 with high visible-light photocatalytic activity, J. Environ. Chem. Eng. 3 (2) (2015) 603–608.
[60] Luigi Da Vià, Carlo Recchi, Edgar O. Gonzalez-Yañez, Thomas E. Davies, Jose A. Lopez-Sanchez, Visible light selective photocatalytic conversion of glucose by TiO_2, Appl. Catal. B 202 (2017) 281–288.
[61] R.D. Shannon, J.A. Pask, Kinetics of the Anatase-Rutile Transformation, Journal of the American Ceramic Society. 48 (1965) 391–398. https://doi.org/10.1111/j.1151-2916.1965.tb14774.x.
[62] L. Lajaunie, C. Pardanaud, C. Martin, P. Puech, C. Hu, M.J. Biggs, R. Arenal, Advanced spectroscopic analyses on a:C-H materials: Revisiting the EELS characterization and its coupling with multi-wavelength Raman spectroscopy, Carbon 112 (2017) 149–161.
[63] A.S. Marfunin, Physics of Minerals and Inorganic Materials: An Introduction //www.springer.com/gp/book/9783642670466 Springer-Verlag, Berlin Heidelberg, 1979.
[64] Qingwu Huang, Shouqin Tian, Dawen Zeng, Xiaoxia Wang, Wulin Song, Yingying Li, Wei Xiao, Changsheng Xie, Enhanced Photocatalytic Activity of Chemically Bonded TiO 2 /Graphene Composites Based on the Effective Interfacial Charge Transfer through the C–Ti Bond, ACS Catal. 3 (7) (2013) 1477–1485.
[65] Alex Dolgonos, Thomas O. Mason, Kenneth R. Poeppelmeier, Direct optical band gap measurement in polycrystalline semiconductors: A critical look at the Tauc method, J. Solid State Chem. 240 (2016) 43–48.
[66] Ashley M. Pennington, Amanda I. Okonmah, Daryll T. Munoz, George Tsilomelekis, Fuat E. Celik, Changes in Polymorph Composition in P25-TiO 2 during Pretreatment Analyzed by Differential Diffuse Reflectance Spectral Analysis, J. Phys. Chem. C 122 (9) (2018) 5093–5104.
[67] Jinfeng Zhang, Peng Zhou, Jianjun Liu, Jiaguo Yu, New understanding of the difference of photocatalytic activity among anatase, rutile and brookite TiO 2, Phys. Chem. Chem. Phys. 16 (38) (2014) 20382–20386.
[68] Tim Luttrell, Sandamali Halpegamage, Junguang Tao, Alan Kramer, Eli Sutter, Matthias Batzill, Why is anatase a better photocatalyst than rutile? - Model studies on epitaxial TiO_2 films, Sci Rep 4 (1) (2015), https://doi.org/10.1038/srep04043.
[69] N. Serpone, D. Lawless, R. Khairutdinov, Size Effects on the Photophysical Properties of Colloidal Anatase TiO_2 Particles: Size Quantization versus Direct Transitions in This Indirect Semiconductor? J. Phys. Chem. 99 (45) (1995) 16646–16654.
[70] K Madhusudan Reddy, Sunkara V Manorama, A Ramachandra Reddy, Bandgap studies on anatase titanium dioxide nanoparticles, Mater. Chem. Phys. 78 (1) (2003) 239–245.
[71] Katarzyna Anna Michalow, Dmitry Logvinovich, Anke Weidenkaff, Martin Amberg, Giuseppino Fortunato, Andre Heel, Thomas Graule, Mieczyslaw Rekas, Synthesis, characterization and electronic structure of nitrogen-doped TiO_2 nanopowder, Catal. Today 144 (1-2) (2009) 7–12.
[72] M Koelsch, S Cassaignon, J.F Guillemoles, J.P Jolivet, Comparison of optical and electrochemical properties of anatase and brookite TiO2 synthesized by the sol–gel method, Thin Solid Films 403-404 (2002) 312–319.
[73] Toshiaki Ohsaka, Fujio Izumi, Yoshinori Fujiki, Raman spectrum of anatase, TiO_2, J. Raman Spectrosc. 7 (6) (1978) 321–324.
[74] Andrea C. Ferrari, Denis M. Basko, Raman spectroscopy as a versatile tool for studying the properties of graphene, Nature Nanotech 8 (4) (2013) 235–246.
[75] Corrado Garlisi, Gabriele Scandura, Jakub Szlachetko, Sareh Ahmadi, Jacinto Sa,

Giovanni Palmisano, E-beam evaporated TiO 2 and Cu-TiO 2 on glass: Performance in the discoloration of methylene blue and 2-propanol oxidation, Appl. Catal. A 526 (2016) 191–199.
[76] D. Dvoranová, Z. Barbieriková, V. Brezová, Radical Intermediates in Photoinduced Reactions on TiO2 (An EPR Spin Trapping Study), Molecules. 19 (2014) 17279–17304. https://doi.org/10.3390/molecules191117279.
[77] Lizhong Wang, Shuxin Ouyang, Bofan Ren, Jinhua Ye, Defa Wang, Enhanced photocatalytic degradation of 2-propanol over macroporous GaN/ZnO solid solution prepared by a novel sol-gel method, APL Mater. 3 (10) (2015) 104414, https://doi.org/10.1063/1.4928702.
[78] Weizong Xu, Daniel Raftery, Photocatalytic Oxidation of 2-Propanol on TiO 2 Powder and TiO 2 Monolayer Catalysts Studied by Solid-State NMR, J. Phys. Chem. B 105 (19) (2001) 4343–4349.
[79] Colin F. Chignell, Ann G. Motten, Robert H. Sik, Carol E. Parker, Krzysztof Reszka, A SPIN TRAPPING STUDY OF THE PHOTOCHEMISTRY OF 5,5-DIMETHYL-1-PYRROLINE *N* -OXIDE (DMPO), Photochem. Photobiol. 59 (1) (1994) 5–11.
[80] Junbo Zhong, Jianli Wang, Lin Tao, Maochu Gong, Liu Zhimin, Yaoqiang Chen, Photocatalytic degradation of gaseous benzene over TiO_2/Sr_2CeO_4: Kinetic model and degradation mechanisms, J. Hazard. Mater. 139 (2) (2007) 323–331.
[81] Vincenzo Augugliaro, Marianna Bellardita, Vittorio Loddo, Giovanni Palmisano, Leonardo Palmisano, Sedat Yurdakal, Overview on oxidation mechanisms of organic compounds by TiO_2 in heterogeneous photocatalysis, J. Photochem. Photobiol., C 13 (3) (2012) 224–245.
[82] Ralph G. Pearson, Absolute electronegativity and hardness: application to inorganic chemistry, Inorg. Chem. 27 (4) (1988) 734–740.
[83] Yong Xu, Martin A.A. Schoonen, The absolute energy positions of conduction and valence bands of selected semiconducting minerals, Am. Mineral. 85 (3-4) (2000) 543–556.
[84] Shi-Jun Liang, L. K. Ang, Electron Thermionic Emission from Graphene and a Thermionic Energy Converter, Phys. Rev. Applied 3 (1) (2015), https://doi.org/10.1103/PhysRevApplied.3.014002.
[85] Janusz Lasek, Yi-Hui Yu, Jeffrey C.S. Wu, Removal of NOx by photocatalytic processes, J. Photochem. Photobiol., C 14 (2013) 29–52.
[86] J.S Dalton, P.A Janes, N.G Jones, J.A Nicholson, K.R Hallam, G.C Allen, Photocatalytic oxidation of NO x gases using TiO 2 : a surface spectroscopic approach, Environ. Pollut. 120 (2) (2002) 415–422.
[87] Yoshihisa Ohko, Yuri Nakamura, Akari Fukuda, Sadao Matsuzawa, Koji Takeuchi, Photocatalytic Oxidation of Nitrogen Dioxide with TiO 2 Thin Films under Continuous UV-Light Illumination, J. Phys. Chem. C 112 (28) (2008) 10502–10508.
[88] V. Loddo, G. Marcì, G. Palmisano, S. Yurdakal, M. Brazzoli, L. Garavaglia, L. Palmisano, Extruded expanded polystyrene sheets coated by TiO_2 as new photocatalytic materials for foodstuffs packaging, Appl. Surf. Sci. 261 (2012) 783–788.
[89] M.E. Jenkin, J.C. Young, A.R. Rickard, The MCM v3.3.1 degradation scheme for isoprene, Atmospheric Chemistry and Physics. 15 (2015) 11433–11459. https://doi.org/10.5194/acp-15-11433-2015.
[90] William A. Jacoby, Daniel M Blake, John A. Penned, James E. Boulter, LeAnn M. Vargo, Marya C George, Suzanne K. Dolberg, Heterogeneous Photocatalysis for Control of Volatile Organic Compounds in Indoor Air, J. Air Waste Manag. Assoc. 46 (9) (1996) 891–898.
[91] Olga d'Hennezel, Pierre Pichat, David F Ollis, Benzene and toluene gas-phase photocatalytic degradation over H2O and HCL pretreated TiO_2: by-products and mechanisms, J. Photochem. Photobiol., A 118 (3) (1998) 197–204.
[92] Lung-Chuan Chen, Guan-Ting Pan, Thomas C.-K. Yang, Tsair-Wang Chung, Chao-Ming Huang, In situ DRIFT and kinetic studies of photocatalytic degradation on benzene vapor with visible-light-driven silver vanadates, J. Hazard. Mater. 178 (1-3) (2010) 644–651.
[93] Alastair C. Lewis, The changing face of urban air pollution, Science 359 (6377) (2018) 744–745.
[94] Norman N. Lichtin, Mahmoud Sadeghi, Oxidative photocatalytic degradation of benzene vapor over TiO_2, J. Photochem. Photobiol., A 113 (1) (1998) 81–88.
[95] C.H. Ao, S.C. Lee, C.L. Mak, L.Y. Chan, Photodegradation of volatile organic compounds (VOCs) and NO for indoor air purification using TiO_2: promotion *versus* inhibition effect of NO, Appl. Catal. B 42 (2) (2003) 119–129.